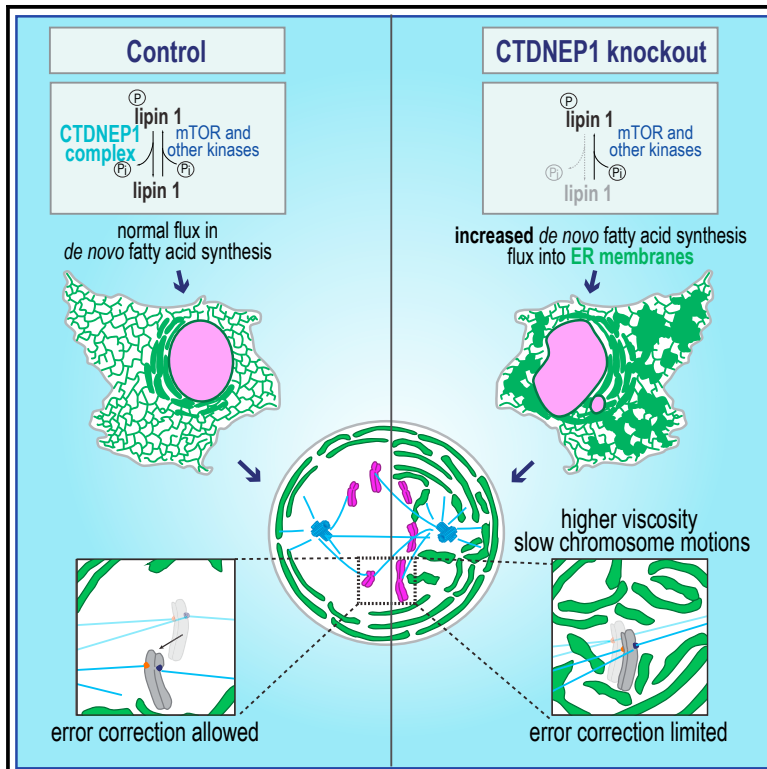# Developmental Cell

Cell cycle regulation of ER membrane biogenesis protects against chromosome missegregation

Graphical abstract

Authors

Holly Merta,
Jake W. Carrasquillo Rodríguez,
Maya I. Anjur-Dietrich, ...,
Thurl E. Harris, Daniel J. Needleman,
Shirin Bahmanyar

Correspondence

shirin.bahmanyar@yale.edu

In brief

Restructuring of the endoplasmic reticulum (ER) is required for mitotic fidelity. Merta, Carrasquillo Rodriguez et al. show that cell cycle regulation of a lipid synthesis enzyme restricts ER proliferation, thus, protecting against mitotic errors. Excess ER membranes can alter the biophysical properties of mitotic cells to cause chromosome missegregation.

Highlights

- Increased fatty acid synthesis can lead to ER expansion and micronuclei formation

- CTDNEP1 regulation of lipin 1 in interphase limits ER expansion and micronuclei

- CTDNEP1 counteracts mTOR phosphorylation of lipin 1 in interphase

- Excess ER membranes inherited by mitotic cells impede error correction

CellPress

Developmental Cell

CellPress

Article

Cell cycle regulation of ER membrane biogenesis protects against chromosome missegregation

Holly Merta,[1,6] Jake W. Carrasquillo Rodríguez,[1,6] Maya I. Anjur-Dietrich,[2] Tevis Vitale,[1] Mitchell E. Granade,[3] Thurl E. Harris,[3] Daniel J. Needleman,[2,4,5] and Shirin Bahmanyar[1,7,*]

[1]Department of Molecular, Cellular and Developmental Biology, Yale University, New Haven, CT 06511, USA
[2]Department of Applied Physics, School of Engineering and Applied Sciences, Harvard University, Cambridge, MA 02138, USA
[3]Department of Pharmacology, University of Virginia, Charlottesville, VA 22908, USA
[4]Department of Molecular and Cellular Biology, Harvard University, Cambridge, MA 02138, USA
[5]Center for Computational Biology, Flatiron Institute, New York, NY 10010, USA
[6]These authors contributed equally
[7]Lead contact
*Correspondence: shirin.bahmanyar@yale.edu
https://doi.org/10.1016/j.devcel.2021.11.009

SUMMARY

Failure to reorganize the endoplasmic reticulum (ER) in mitosis results in chromosome missegregation. Here, we show that accurate chromosome segregation in human cells requires cell cycle-regulated ER membrane production. Excess ER membranes increase the viscosity of the mitotic cytoplasm to physically restrict chromosome movements, which impedes the correction of mitotic errors leading to the formation of micronuclei. Mechanistically, we demonstrate that the protein phosphatase CTDNEP1 counteracts mTOR kinase to establish a dephosphorylated pool of the phosphatidic acid phosphatase lipin 1 in interphase. CTDNEP1 control of lipin 1 limits the synthesis of fatty acids for ER membrane biogenesis in interphase that then protects against chromosome missegregation in mitosis. Thus, regulation of ER size can dictate the biophysical properties of mitotic cells, providing an explanation for why ER reorganization is necessary for mitotic fidelity. Our data further suggest that dysregulated lipid metabolism is a potential source of aneuploidy in cancer cells.

INTRODUCTION

The endoplasmic reticulum (ER) is a large membrane-bound organelle composed of interconnected membrane sheets and tubules that are continuous with the nuclear envelope (NE) (Baumann and Walz, 2001; Friedman and Voeltz, 2011). In animal cells, ER membranes are spread throughout the cytoplasm extending from the NE along the microtubule (MT) cytoskeleton to the cell periphery (English and Voeltz, 2013). The ER loses most of its interactions with MTs in mitosis (Smyth et al., 2012; Wang et al., 2013), and NE/ER membranes undergo extensive remodeling to become excluded from the region occupied by the mitotic spindle in metaphase (Champion et al., 2017; Liu and Pellman, 2020; Lu et al., 2011; Puhka et al., 2012, 2007). The mechanisms that drive ER membrane exclusion from mitotic spindle MTs are not fully understood; however, both active mechanisms, mediated by the minus-end MT motor dynein (Turgay et al., 2014) and by the ER tubule shaping proteins REEP3/4 (Kumar et al., 2019; Schlaitz et al., 2013), and passive mechanisms, resulting from loss of MT-ER interactions, are involved (Liu and Pellman, 2020).

Little is known about the significance of the spatial reorganization of ER membranes in mitosis. The remodeling of ER membranes and their location away from the mitotic spindle

may facilitate equal partitioning of the ER to daughter cells (Champion et al., 2017). Some evidence also suggests that the ER surrounding spindle MTs serves as part of an organelle-exclusion "spindle envelope" that spatially confines mitotic proteins to the spindle region (Schweizer et al., 2015). Several studies further show that persistent ER membrane contacts with mitotic chromosomes, but not with spindle MTs, correlate with higher incidences of chromosome missegregation (Champion et al., 2019; Luithle et al., 2020; Schlaitz et al., 2013; Smyth et al., 2012).

The need for ER membranes to be excluded from the spindle region may be met by restricting the production of ER membranes prior to cell entry into mitosis. The accumulation of membrane glycerophospholipids increases in interphase (Habenicht et al., 1985; Jackowski, 1994), but whether ER membrane synthesis is coupled to ER membrane reorganization in mitosis has not been tested.

To understand if there is a role for cell cycle regulation of ER membrane biogenesis to ensure its mitotic reorganization, we focused on the highly conserved but understudied human serine/threonine (S/T) protein phosphatase CTDNEP1 (C-terminal domain nuclear envelope phosphatase 1), which forms a complex with NEP1R1 (Spo7p in budding yeast/NEPR-1 in *C. elegans*) to dephosphorylate a key enzyme in lipid synthesis,
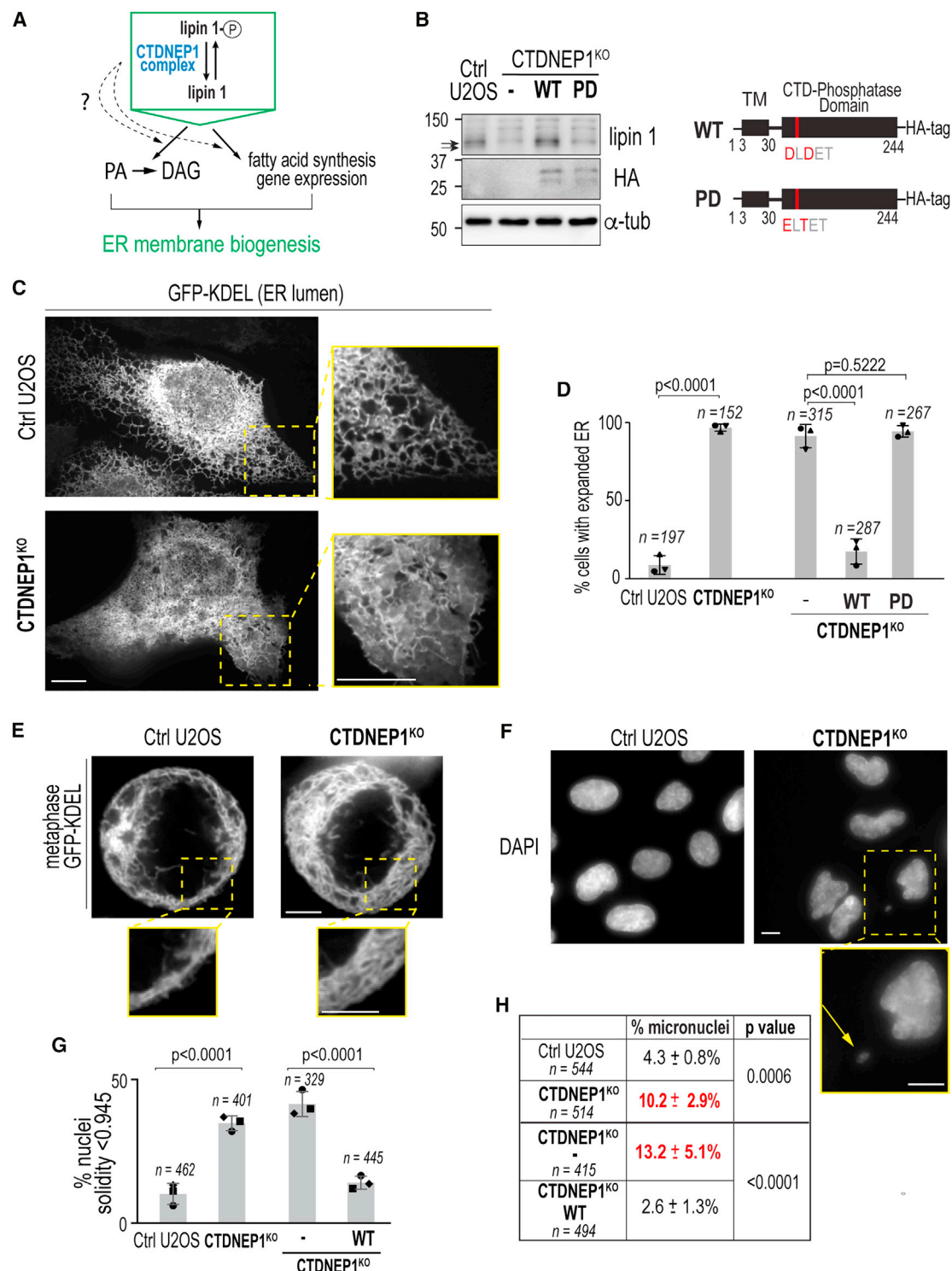
Figure 1. ER membrane expansion and formation of micronuclei in the absence of CTDNEP1

(A) Schematic of CTDNEP1 regulation of lipin 1.

(B) Immunoblot of whole cell lysates of indicated conditions. Arrows, lipin 1 phospho-species. Right: schematic of wild type (WT) and phosphatase-dead (PD) human CTDNEP1.

(C) Spinning disk confocal images in indicated cells.

(D) Plot, % of cells with indicated phenotypes analyzed live with GFP-KDEL (left two) or in fixed cells with calnexin staining (right three).

(E) Spinning disk confocal images in indicated metaphase cells.

(legend continued on next page)

Developmental Cell
Article

CellPress

lipin 1 (Pah1p in budding yeast/Ned1 in fission yeast/LPIN-1 in *C. elegans*) (Han et al., 2012; Kim et al., 2007). Work in non-mammalian model systems demonstrated that CTDNEP1 (Nem1p in fission and budding yeasts/CNEP-1 in *C. elegans*) regulation of lipin impacts mitotic processes (Bahmanyar et al., 2014; Han et al., 2012; O'Hara et al., 2006; Siniossoglou et al., 1998; Tange et al., 2002; Zhang and Reue, 2017). CTDNEP1[Nem1] control of lipin has a role in expansion of the NE necessary to accommodate the elongating mitotic spindle in closed mitosis of budding and fission yeasts (Makarova et al., 2016; Witkin et al., 2012). In *C. elegans* embryos, CTDNEP1[CNEP-1] restricts ER expansion through regulation of lipin to facilitate the breakdown and fusion of pronuclear membranes (Bahmanyar et al., 2014). Some evidence also suggests that lipid signaling by CTDNEP1/lipin facilitates NE breakdown in open mitosis of human cells (Mall et al., 2012). However, a role for CTDNEP1/lipin in mitotic ER reorganization in mammalian cells has not been shown, although the fact that CTDNEP1 qualifies as a candidate for the long sought-after tumor suppressor in Group 3/4 medulloblastomas (Jones et al., 2012; Northcott et al., 2012) further motivated its functional analysis in human cells.

Human CTDNEP1 with its binding partner NEP1R1 dephosphorylates lipin proteins when overexpressed (Han et al., 2012), but a direct link to endogenous lipin 1 dephosphorylation and how this relates to ER lipid synthesis has not been shown. Lipin proteins are peripheral membrane binding, Mg^{2+}-dependent phosphatidic acid phosphatases that catalyze the conversion of phosphatidic acid (PA) to diacylglycerol (DAG) on the outer leaflet of the ER (Zhang and Reue, 2017). PA and DAG are precursors for the production of the membrane glycerolipids (phosphatidylcholine [PC], phosphatidylethanolamine [PE], and phosphatidylinositol [PI]), as well as triglycerides (Fagone and Jackowski, 2009). There are three lipins in mammalian cells, and lipin 1 (expressed as isoforms α, β, and γ) has the highest phosphatic acid phosphatase (PAP) activity (Donkor et al., 2007). Lipin 1 is phosphorylated at multiple S/T sites, at least 19 of which are known to increase its catalytic activity *in vitro* when mutated to alanine (Eaton et al., 2013). The relevance of lipin 1 phosphorylation to its local activity toward PA within cells is not well-understood (Zhang and Reue, 2017).

Lipin 1 can also translocate into the nucleus to control the expression of genes required for lipid metabolism (Finck et al., 2006; Harris and Finck, 2011; Péterfy et al., 2005; Peterson et al., 2011; Zhang and Reue, 2017). Direct phosphorylation of lipin 1 by the nutrient-sensing kinase mTORC1 promotes its enrichment in the cytoplasm allowing the transcription of genes encoding for fatty acid (FA) synthesis enzymes by Sterol Regulatory Element Binding Protein 1 (SREBP1) (Peterson et al., 2011). It has been predicted that CTDNEP1/NEP1R1 complex dephosphorylates a mTORC1-directed phosphorylation site on lipin 1 (Wu et al., 2011); however, a direct demonstration of counteracting activities for CTDNEP1 phosphatase and mTOR kinase on lipin 1 is lacking. Lipin 1 is also hyperphosphorylated in mitosis, when mTORC1 is inactive (Odle et al., 2020), on consensus sites

for cyclin-dependent kinase 1 (Cdk1) (Grimsey et al., 2008). The Mg^{2+}-dependent PAP activity is lower in mitotic cells (Grimsey et al., 2008); however, the significance of the mitotic phosphorylation of lipin 1 is not well-understood.

Here, we show that human CTDNEP1 regulation of lipin 1 limits *de novo* FA synthesis to restrict ER membrane biogenesis specifically in interphase. When CTDNEP1 is absent, prometaphase cells inherit expanded ER membranes, which increase the viscosity of the mitotic cytoplasm and slow chromosome movements. The slower mobility of chromosomes impairs the correction of mitotic errors and increases the incidence of cells that contain micronuclei. We demonstrate that CTDNEP1 counteracts mTOR-mediated phosphorylation of lipin 1 to establish and maintain a dephosphorylated pool of lipin 1 in interphase. The absence of this dephosphorylated pool makes lipin 1 less stable and corresponds to an increase in *de novo* FA synthesis. Inhibition of a rate-limiting enzyme for FA synthesis upregulated in CTDNEP1 knockout cells suppresses both the expansion of the ER in interphase cells and the formation of micronuclei. Thus, the regulation of ER membrane production in interphase by CTDNEP1/lipin 1 is required for mitotic fidelity.

RESULTS

CTDNEP1 regulation of lipin 1 restricts ER membrane proliferation

The conserved integral membrane protein phosphatase CTDNEP1 dephosphorylates lipin in all organisms tested (Bahmanyar et al., 2014; Kim et al., 2007; O'Hara et al., 2006); however, almost nothing is known about CTDNEP1's role in regulation of lipin 1 to control ER membrane biogenesis in mammalian cells (Figure 1A). We found that a genome-edited homozygous clonal U2OS knockout cell line for CTDNEP1 and cells subjected to RNAi-mediated depletion of CTDNEP1 contain reduced levels of lipin 1 protein as well as the absence of a faster migrating product (Figures 1B and S1A–S1C). Treatment with exogenous lambda phosphatase resulted in an electrophoretic mobility shift of lipin 1 to a faster migrating species in both wild type (WT) and knockout cells (Figure S1D), indicating that lipin 1 is in a mostly phosphorylated form in CTDNEP1 knockout cells. Stable expression of WT CTDNEP1, but not a catalytically inactive version (PD, phosphatase dead) (Kim et al., 2007; Seifried et al., 2013), restored both lipin 1 levels and phosphorylation states (Figure 1B). Thus, catalytically active human CTDNEP1 is required to maintain a dephosphorylated pool of lipin 1 and may be required to stabilize lipin 1 protein levels.

The ER phenotype following a penetrant RNAi-depletion of lipin 1 was distinct from CTDNEP1 knockout cells (Figures 1C, S1E, and S1F). The morphology of the peripheral ER was severely altered without lipin 1—instead of a uniform tubular network, ER membranes formed sparse tubules and interspersed sheet-like structures (Figure S1F). In contrast, there was an overabundance of ER membranes in interphase and mitotic CTDNEP1 knockout cells, which was confirmed by lipid

(F) Epifluorescence images of nuclei in indicated cells. Inset: micronucleus (arrow).

(G) Plot, incidence of nuclei with solidity value <1 SD from control mean solidity. Data in right two and left two bars are from separate experiments.

(H) Incidence of micronuclei in indicated cells. For all: scale bars, 10 μm. Mean ± SDs shown (3 experimental repeats). p values, Fisher's exact tests. See also Figures S1 and S2.
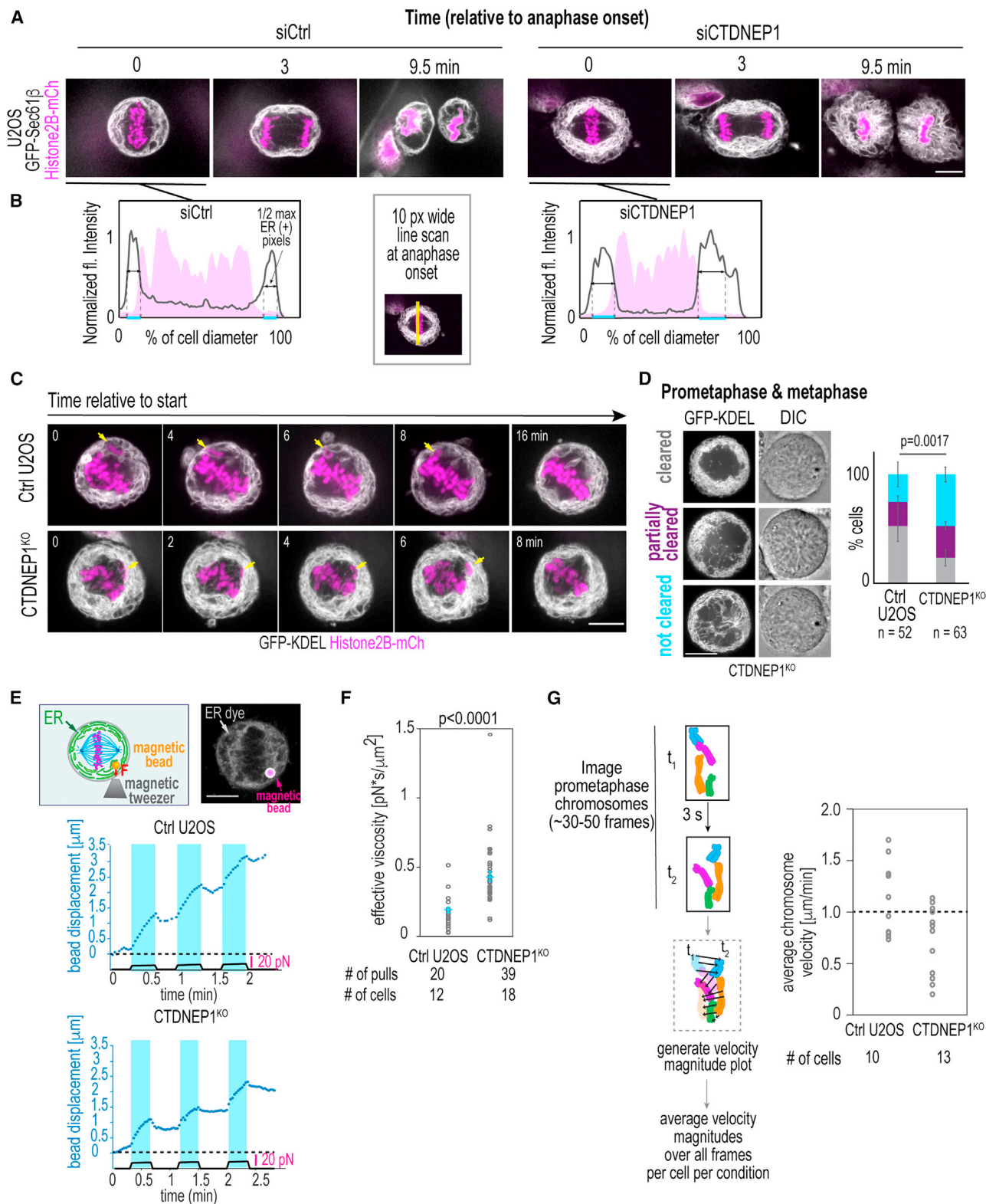
Figure 2. Expanded ER membranes, increased effective viscosity, and diminished chromosome dynamics of CTDNEP1 deleted mitotic cells

(A) Selected spinning disk confocal time lapse images in cells treated as indicated.

(B) Plots, line profiles of fluorescent intensities along region shown.

(C) Selected spinning disk confocal time lapse images in indicated cells after recovery from Cdk1i. Arrows, unaligned chromosomes.

Developmental Cell
Article

CellPress

mass spectrometry analysis of asynchronous cells as an increase in the levels of the major membrane glycerophospholipids (PC and PE) (Figures 1C–1E, S1G and S1H; Table S1). This expansion of the ER membrane network was also observed with an endogenous ER marker in fixed CTDNEP1 knockout cells (Figure S2A) and in U2OS and RPE-1 cells RNAi-depleted for CTDNEP1, but not U2OS cells depleted of lipin 1 (Figures S2B–S2E).

In agreement with the importance of dephosphorylating lipin 1 to control ER membrane biogenesis, overexpression of a catalytically active mouse lipin 1β with 19 S/T sites mutated to alanine (Peterson et al., 2011) was sufficient to suppress the expanded ER phenotype resulting from loss of CTDNEP1 (Figure S2F), whereas overexpression of WT lipin 1β only partially restored the altered ER appearance (Figure S2F). This result combined with the fact that a penetrant RNAi-depletion of lipin 1 results in a distinct phenotype from CTDNEP1 knockout cells suggested that regulation of the phosphorylation state of lipin 1 by CTDNEP1 controls ER membrane biogenesis in mammalian cells. In line with this, *in vitro* measurements showed that Mg^{2+}-dependent PAP activity is retained in CTDNEP1 knockout cells (Figures S2G and S2H), suggesting that these cells contain lipin 1 enzyme activity, albeit at a lower level than control cells. Furthermore, there is an increase in the incorporation of radiolabeled acetate into lipids in CTDNEP1 knockout cells indicating an increased flux of *de novo* synthesized FAs towards membrane biosynthesis (Figure S2I). We conclude that a greater flux of FAs into glycerophospholipid synthesis overrides the partial reduction in overall lipin 1 levels and activity that occurs in CTDNEP1 knockout cells to lead to ER membrane expansion.

CTDNEP1 knockout cells contain micronuclei

We found a conserved requirement for human CTDNEP1 in maintenance of nuclear structure (Figures 1F and 1G) (Bahmanyar et al., 2014; Fonseca et al., 2019; Siniossoglou et al., 1998); while measuring nuclear morphology, we frequently observed primary nuclei with micronuclei in interphase CTDNEP1 knockout cells, and this phenotype was restored by stable expression of CTDNEP1-HA (Figures 1F, inset, and 1H). Micronuclei form because of improper attachment of spindle MTs to kinetochores that lead to lagging chromosomes in anaphase (Cimini, 2008; Liu and Pellman, 2020). Thus, the increased incidence of micronuclei in CTDNEP1 knockout cells may be related to excessive ER membranes interfering with some aspect of mitotic chromosomes and their ability to attach to spindle MTs.

Expanded ER membranes increase the viscosity of the mitotic cytoplasm and slow chromosome motions

Live imaging to monitor ER occupancy from anaphase onset to mitotic exit revealed that a consistently greater percentage of the cell diameter was taken up by ER membranes in CTDNEP1 RNAi-depleted or knockout cells (Figures 2A, 2B, and S3A–

S3C; Video S1), and this corresponded to a smaller region occupied by mitotic chromosomes (Figures 2A and 2B). We next imaged synchronized cells in prometaphase to assess the spatial organization of ER membranes in relation to unaligned chromosomes (Figure 2C, arrows; Video S2). In both control U2OS and CTDNEP1 knockout cells in prometaphase, an unaligned chromosome was observed within the peripheral ER network before moving toward the metaphase plate (Figure 2C, arrows; Video S2); however, unlike control U2OS cells, CTDNEP1 knockout cells also contained some ER membranes mislocalized to the spindle region (Figure 2C; Video S2). To quantify the incidence of ER membranes invading the spindle region, we enriched for prometaphase and metaphase cells by performing a drugless mitotic shake off directly followed by live imaging (Figure 2D). Our phenotypic scoring revealed a significant proportion of CTDNEP1 knockout cells with ER membranes in the region occupied by mitotic chromosomes as assessed by DIC (Figure 2D). Thus, when CTDNEP1 is absent, excessive ER membranes occupy a larger area of the peripheral mitotic cytoplasm and aberrantly invade the region where mitotic chromosomes are located.

We hypothesized that an expanded occupancy of the ER in prometaphase may contribute to viscous forces exerted on mitotic chromosomes. This idea predicts that mitotic chromosomes entrapped by the peripheral ER network would have slower short-range movements, which could impede the proper attachment of dynamic spindle MTs to kinetochores (Cimini et al., 2003). To test this idea, we monitored the displacement of magnetic beads approximately the size of a mitotic chromosome (~2–3 μm) in the periphery of mitotic cells in response to a constant force applied with magnetic tweezers (Figure 2E; Video S3). In control U2OS cells, the displacement of a magnetic bead in response to a constant force of ~10 pN for ~20 s was ~1.5 μm (Figure 2E, top plot). In contrast, in CTDNEP1 knockout cells, a similar force regime resulted in bead displacement of less than 1 μm (Figure 2E, bottom). These data revealed a two-fold increase in the effective viscosity of the mitotic cytoplasm of CTDNEP1 knockout cells compared with control U2OS cells (Figure 2F; 0.43 ± 0.04 pN * s/μm² in CTDNEP1 knockout compared with 0.19 ± 0.02 pN * s/μm² in control U2OS cells). High temporal resolution imaging of fluorescently labeled prometaphase chromosomes revealed a greater proportion of CTDNEP1 knockout cells with an average chromosome velocity of less than 1 μm/ min (10/13 CTDNEP1 knockout cells compared with 5/10 control U2OS cells having an average magnitude velocity of <1 μm/ min; Figures 2G and S3D; Video S4). The reduction in the displacements of mitotic chromosomes in CTDNEP1 knockout cells also suggests an explanation for the more compact occupancy of mitotic chromosomes at anaphase onset (Figure 2B). We conclude that when ER membranes are in excess they are more prone to persist in the area occupied by prometaphase chromosomes, effectively increasing the surrounding viscosity to cause slower chromosome motions.

(D) Center plane spinning disk confocal images of mitotic cells. Plot, incidence of phenotypes. Means ± SDs shown. 3 experimental repeats. p value, χ^2 test.
(E) Top: schematic of experiment setup and confocal image of ER (gray) and magnetic bead (magenta) in a mitotic U2OS cell. Plots, applied force (black solid line) and bead displacement (blue dotted line).
(F) Plot of effective cytoplasmic viscosity in indicated cells. Means ± SEM shown. p value, unpaired t test with Welch's correction.
(G) Schematic (left) for quantifying average velocity magnitudes for chromosomes for indicated cells in plot (right). For all, scale bars, 10 μm. See also Figure S3.

Micronucleation in CTDNEP1 knockout cells results from a reduction in mitotic error correction

The slow motions of mitotic chromosomes in prometaphase might increase errors in MT-chromosome attachments, which would account for the increased incidence of micronuclei formation we observed in CTDNEP1-deleted cells. Inhibition of the spindle assembly checkpoint (SAC) serves as a readout for the rate of attachment errors because cells enter anaphase without resolving improperly attached or unattached kinetochores (Liu and Pellman, 2020). This results in a substantial increase in the frequency of chromosome missegregation events and micronucleation. To test if loss of CTDNEP1 enhances the frequency of erroneous attachments, we released cells synchronized in G2/M in the presence of an inhibitor to MPS1 (MPS1i), the mitotic kinase that activates the SAC (Figure 3A, "SAC override"; Liu et al., 2018). 39.9% ± 1.9% of control cells were micronucleated, reflecting the rate of unresolved errors in attachment prior to entry into anaphase, whereas 43.3% ± 4.9% of CTDNEP1 knockout cells were micronucleated (Figures 3B and 3C). Although this increase was significant, the difference in the percentage of micronuclei between control and knockout cells is small, suggesting that an increased incidence of errors in MT attachments to kinetochores may not be the major source of micronucleation observed in CTDNEP1-deleted cells.

Another possibility is that the slow motions of mitotic chromosomes impede the correction of errors in MT-chromosome attachments to cause chromosome missegregation and formation of micronuclei in CTDNEP1-deleted cells. Transient spindle disassembly by washout from nocodazole treatment increases the frequency of merotelic attachments in which a single kinetochore is attached to MTs from both spindle poles instead of just one (Cimini et al., 2003) (Figure 3D). Unlike other mis-attachments, merotelic attachments are not detected by the SAC; however, MT dynamics and chromosomal movements that promote biorientation substantially reduce these improper attachments prior to anaphase onset resulting in a modest, albeit significant, increase in lagging chromosomes and micronucleation after nocodazole washout (Cimini, 2008; Cimini et al., 2003) (Figure 3D). Transient spindle disassembly led to the expected increase in micronucleation in control U2OS cells (Figures 3E and 3F; compare 10.6% ± 2.0% in Figure 3F to 4.3% ± 0.8% in Figure 1H) (Cimini et al., 2003; Liu et al., 2018), whereas a significant percentage of CTDNEP1 knockout cells were severely micronucleated—in addition to one or two small micronuclei, these cells contained multiple severely multilobed nuclei (hereafter referred to as "hyper-micronucleation"; 40.0% ± 8.5% in CTDNEP1 knockout compared with 4.3% ± 1.2% in control, Figures 3E and 3F). We also observed more instances of chromosomes separated from the main mass after recovery from nocodazole treatment in telophase of CTDNEP1 knockout cells when compared with control (Figure 3G), consistent with the hyper-micronucleation phenotype resulting from errors in chromosome segregation. Importantly, the hyper-micronucleation phenotype was suppressed upon stable expression of CTDNEP1-HA (Figure 3F) and was also observed in RPE-1 cells RNAi-depleted for CTDNEP1 (Figures S4A and S4B). Taken together, these data suggest that merotelic attachments go uncorrected in CTDNEP1 knockout cells, leading to lagging chromosomes in anaphase that form micronuclei.

Micronucleation in CTDNEP1 knockout cells is suppressed by expression of a constitutively dephosphorylated lipin 1

We reasoned that if the hyper-micronucleation phenotype in CTDNEP1 knockout cells results from expanded ER membranes impairing chromosome movements, then expression of a constitutively dephosphorylated form of lipin 1 that suppresses ER expansion in these cells (Figure S2F) should also suppress hyper-micronucleation. Overexpression of a catalytically active mouse lipin 1β with 19 S/T sites mutated to alanine suppressed the hyper-micronucleation phenotype resulting from loss of CTDNEP1 (8.7% ± 1.0% with FLAG-lipin 1β 19xA compared with 30.7% ± 1.4% in control; 26.2% ± 2.8% with phosphatase-dead FLAG-lipin 1β 19xA compared with 25.3% ± 3.4% in control, Figure 3F). These data suggested that CTDNEP1 restricts ER membrane biogenesis through dephosphorylation of catalytically active lipin 1 so that mitotic cells inherit a less dense ER network, which allows mitotic error correction and prevents formation of micronuclei.

CTDNEP1 is necessary to establish and maintain a stable, dephosphorylated pool of lipin 1 in interphase by counteracting mTOR

Our data demonstrating that expression of lipin 1β with 19 S/T phosphorylation sites mutated to alanine, which includes the sites targeted by mTOR complex 1 (Peterson et al., 2011), is sufficient to restore the ER expansion (Figure S2F), and hyper-micronucleation (Figure 3F) phenotypes of CTDNEP1 knockout cells prompted us to test if CTDNEP1 maintains a dephosphorylated pool of lipin 1 by counteracting phosphorylation of lipin 1 by mTOR kinase. mTOR-mediated phosphorylation of lipin 1 controls lipid homeostasis by limiting the nuclear localization of lipin 1. Less lipin 1 localized to the nucleus allows SREBP1-dependent expression of genes encoding for enzymes in the *de novo* FA synthesis pathway (Lamming and Sabatini, 2013; Peterson et al., 2011; Shimizu et al., 2017). Evidence also suggests that mTOR regulates lipin 1 protein stability through the proteasomal degradation pathway (Shimizu et al., 2017).

We first monitored the phosphorylation state of lipin 1 in a time course of asynchronous control and CTDNEP1 knockout cells treated with the mTOR kinase inhibitor Torin 1 (Peterson et al., 2011). Control U2OS cells showed a doublet of endogenous lipin 1 representing its distinct phosphorylation states (Figure 4A). Treating U2OS cells with Torin 1 for 30 min and after up to 12 h caused a shift in the electrophoretic mobility of lipin 1 to the faster migrating, dephosphorylated product consistent with rapid dephosphorylation of lipin 1 in the absence of mTOR kinase activity (Figure 4A). In contrast, the dephosphorylated species of lipin 1 did not appear until 2 h of Torin 1 treatment in CTDNEP1 knockout cells and was present at much lower levels throughout the time course of the experiment when compared with control U2OS cells (Figure 4A). These data suggested that the majority of lipin 1 that becomes dephosphorylated upon inhibition of mTOR kinase activity depends on CTDNEP1.

Inhibition of mTOR kinase by Torin 1 results in translocation of lipin 1 from the cytoplasm to the nucleus (Peterson et al., 2011). Consistent with this, human lipin 1β fused to GFP localized to the nucleus in the majority of Torin 1-treated control U2OS
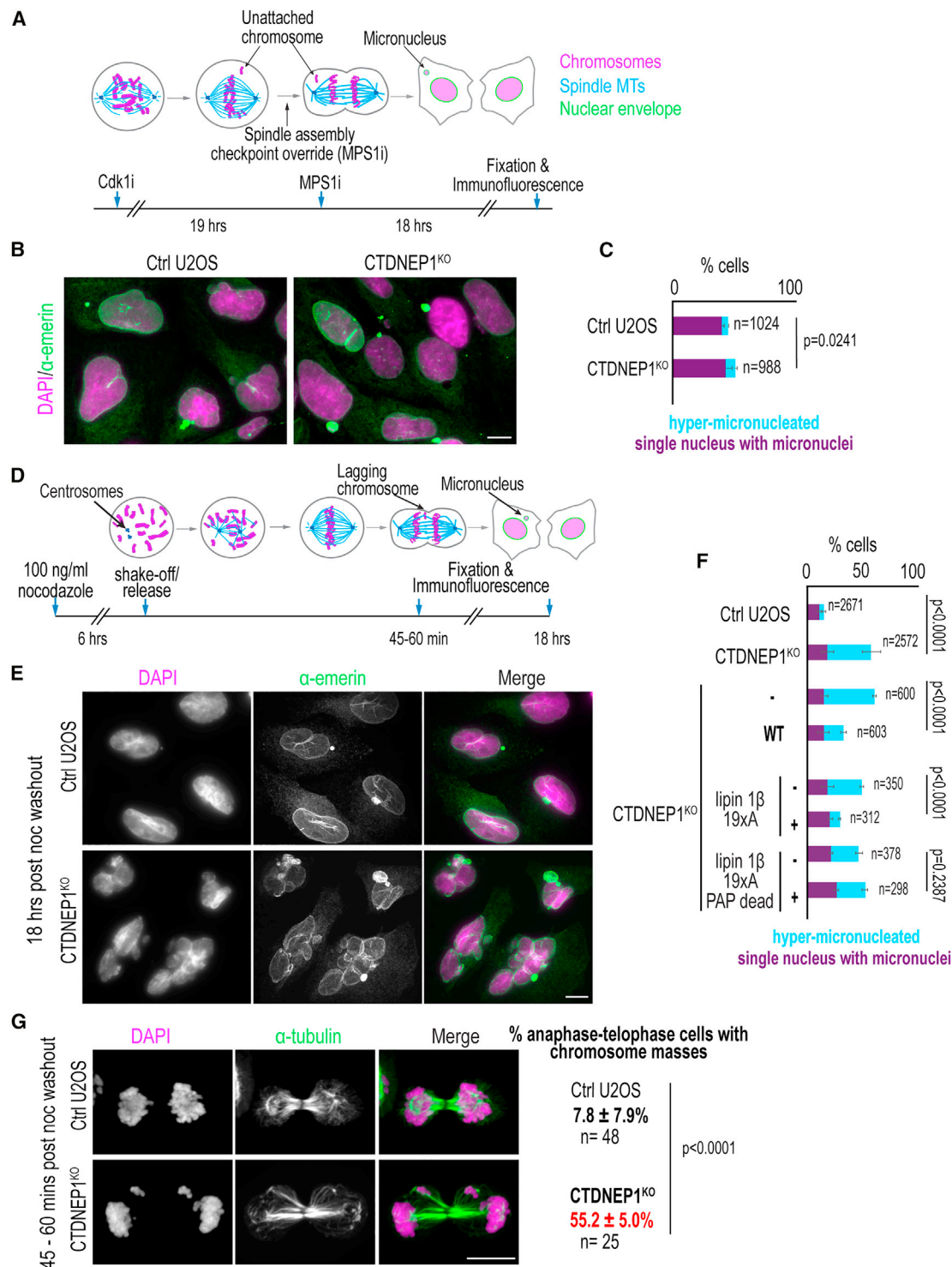
Figure 3. Loss of CTDNEP1 exacerbates the frequency of micronucleation upon transient spindle disassembly

(A) Experimental setup for spindle assembly checkpoint (SAC) inhibition.

(B) Max projection of confocal images in cells treated as in (A).

(C) Incidence of indicated phenotypes in indicated cells.

(D) Experimental setup for transient spindle disassembly.

(E) Max projection of confocal images in indicated cells after treatment as in (D).

(F) Plot of phenotypic incidences in cells treated as indicated.

(G) Max projection of confocal images of cells treated as indicated and incidences of indicated phenotypes. Kinetochore microtubules shown. For all: scale bars, 10 μm. Means ± SDs shown and 3 experimental repeats; p values, χ^2 (C, F) or Fisher's exact (G) test. See also Figure S4.
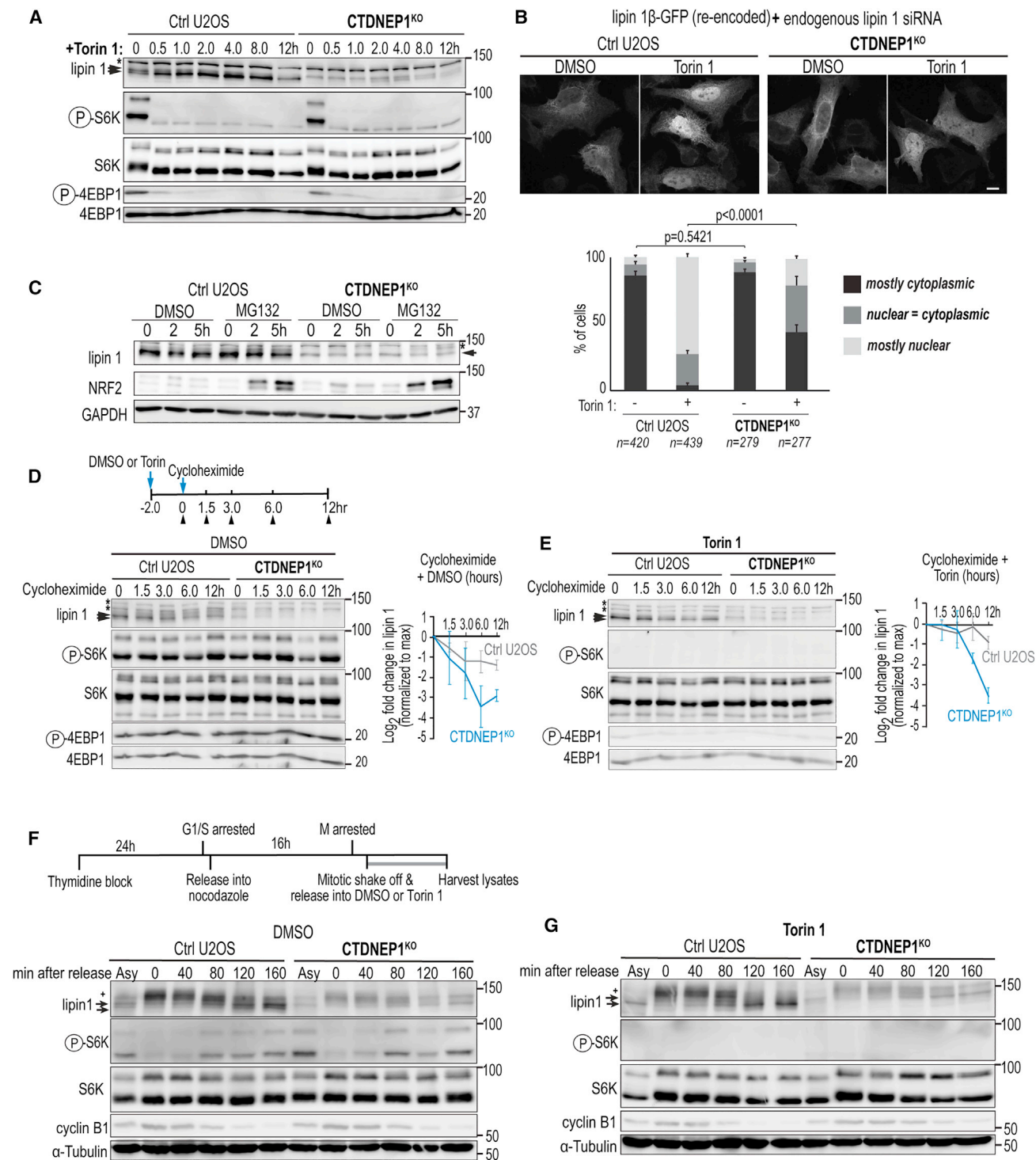
Figure 4. CTDNEP1 counteracts mTOR phosphorylation of lipin 1 in interphase

(A) Immunoblot of lipin 1 from whole cell lysates treated as indicated.

(B) Top: confocal images of fixed cells per indicated conditions. Scale bar, 10μm. Bottom: Plot of nuclear versus cytoplasmic localization of lipin 1 per indicated conditions. p values, χ^2 test.

(C–E) Immunoblot of whole cell lysates from cells treated as indicated. Plots: normalized lipin 1 band intensities in indicated conditions.

(F and G) Above: schematic of mitotic synchronization protocol. Below: immunoblots of whole cell lysates from synchronized cells treated as indicated. For all: Plus signs, lipin 1 mitotic species. Arrowheads, lipin 1 interphase phospho-species; asterisks, non-specific bands. 3 experimental repeats. Means ± SDs shown.

Developmental Cell
Article

CellPress

cells that were selectively RNAi-depleted for endogenous lipin 1 (Figure 4B; Sołtysik et al., 2021). In contrast, lipin 1β-GFP remained mostly cytoplasmic or only partially translocated to the nucleus in Torin 1-treated CTDNEP1 knockout cells (Figure 4B). These data further indicated that CTDNEP1 counteracts mTOR-mediated regulation of lipin 1.

We next tested if CTDNEP1 has a role in stabilizing the levels of lipin 1 protein. Small molecule inhibition of the proteasome with MG132 resulted in the accumulation of a slower-migrating lipin 1 product in CTDNEP1 knockout cells that is likely a hyperphosphorylated species of lipin 1 readily degraded by the proteasome in these cells (Figure 4C). Cycloheximide treatment to prevent new protein translation showed that lipin 1 protein levels are less stable in CTDNEP1 knockout cells (Figure 4D). Torin 1 treatment of CTDNEP1 knockout cells did not fully restore the stability of lipin 1 (Figure 4E). Thus, CTDNEP1 protects lipin 1 protein from proteasomal degradation and it does so by counteracting signals aside from those mediated by mTOR.

To test whether CTDNEP1 is necessary in interphase and/or mitosis to establish a stable, dephosphorylated pool of lipin 1, we monitored the phosphorylation state of endogenous lipin 1 in a time course of control and CTDNEP1 knockout cells released from mitotic arrest. The prominent form of lipin 1 in mitosis is a slow-migrating, hyperphosphorylated species, hereafter referred to as "mitotic lipin 1" (Grimsey et al., 2008) (Figures 4F and 4G). The electrophoretic mobility of mitotic lipin 1 does not depend on the presence of CTDNEP1 (Figure 4F). As cells exited mitosis, the prominent mitotic lipin 1 form transitioned into several faster migrating bands (Figure 4F). When the majority of control cells entered early interphase (~160 min following mitotic release; Figure 4F) lipin 1 protein resolved into two bands resembling the distinct phosphorylation states that were also observed in asynchronous cells (Figure 4F). In contrast, lipin 1 resolved into a single band in CTDNEP1 knockout cells in early interphase that corresponded to the predominant phosphorylated species observed in the asynchronous population of these cells (Figure 4F). Consistent with previous observations that mTORC1 is inactive in mitosis (Odle et al., 2020), inhibition of mTOR kinase activity by Torin 1 did not affect the electrophoretic mobility of mitotic lipin 1 ("0 min," Figure 4G) but resulted in the collapse of lipin 1 into a single dephosphorylated species when the majority of cells had entered interphase (Figure 4G). The emergence of the dephosphorylated lipin 1 species upon mitotic exit in Torin 1-treated cells depended on the presence of CTDNEP1, as in asynchronous cells (Figures 4F and 4G). Thus, CTDNEP1 is necessary to establish a dephosphorylated pool of lipin 1 as cells transition from mitosis to interphase at least in part by counteracting mTOR-mediated phosphorylation of lipin 1. The fact that CTDNEP1 establishes a dephosphorylated pool of lipin 1 in interphase cells but does not impact lipin 1's electrophoretic mobility in mitosis suggested that CTDNEP1 regulates lipin 1 to control ER membrane biogenesis primarily in interphase.

Expanded ER membranes resulting from increased *de novo* FA synthesis during interphase lead to the emergence of micronuclei in CTDNEP1 knockout cells

The interphase state of lipin 1 depends on CTDNEP1 and so we wanted to better understand how this regulatory network might

control ER membrane biogenesis as cells progress through the cell cycle. The increased flux of acetate into total lipids in these cells (Figure S2I) as well as the higher transcript levels of acetyl-CoA carboxylase alpha (ACACA), which catalyzes the committing step for FA synthesis (Figures 5A and S1G), prompted us to test if inhibition of upregulated FA synthesis occurring in these cells would suppress ER expansion. We scored ER morphology of control and knockout cells treated with a small molecule inhibitor that targets ACAC (TOFA, 5′(Tetradecyloxy)-2-furoic acid) (McCune and Harris, 1979), which abolishes *de novo* FA synthesis within 5 h but does not substantially affect the cell cycle even after longer periods of treatment (Figures 5B, S5A, and S5B). In control U2OS cells treated with TOFA, ER membranes were reduced in the majority of cells (Figures 5C, 5D, S5C, and S5D). The addition of exogenous FAs did not alter the morphology of the ER on its own (Figure S5E) but suppressed the altered ER morphology in control U2OS cells treated with TOFA, indicating that the "reduced" ER phenotype results from a reduction in FA synthesis (Figures 5C, 5D, and S5C). TOFA treatment of CTDNEP1 knockout cells suppressed ER expansion resulting in a normal appearance of the ER network, but not with the addition of exogenous FAs (Figures 5C, 5D, S5C, and S5D). TOFA treatment also suppressed abnormal nuclear structure of CTDNEP1 knockout cells (Figure 5E). Thus, the expanded ER phenotype and altered nuclear morphology in CTDNEP1 knockout cells result from excessive incorporation of FAs into ER membrane lipids.

To understand how flux of FAs in the lipid synthesis pathway contributes to ER membrane biogenesis as cells progress through the cell cycle, we determined ER size in cells of different cell cycle stages (Figure S6A). In asynchronous cells, ER area is significantly larger in CTDNEP1 knockout cells than in control cells in S and G2 phases of the cell cycle (Figures S6B and S6C). We synchronized cells in G2/M or G1/S and released them into media containing TOFA to inhibit FA synthesis during either M/G1 phase or S phase, respectively (Figure 6A). The ER area was not significantly altered in cells in G1 phase that were released from synchronization in G2/M into media containing TOFA (Figures 6A–6C, S7A, and S7B). This suggests that ER size is not majorly impacted when FA synthesis is inhibited during mitosis and early G1. In contrast, inhibition of FA synthesis during S-phase significantly reduced the area of the ER in both control and CTDNEP1 knockout cells (Figures 6A–6C, S7A, and S7B). Inhibition of FA synthesis did not affect cell size, excluding the possibility that the reduction in ER area is caused by a reduction in cell size (Figure S7C). These data indicate that FA synthesis contributes to ER membrane biogenesis in S phase. The phosphorylation state of lipin 1 at different stages of interphase was similar to that determined in early interphase and there was less lipin 1 localized to the nucleus in G1 and S phase in CTDNEP1 knockout cells (Figures S7D and S7E). Thus, the extent of ER membrane expansion that occurs in S-phase may be related to the nuclear versus cytoplasmic localization of lipin 1 as determined by CTDNEP1-dependent dephosphorylation of lipin 1 in early interphase (Figures 4F and S7D).

We predicted that if chromosome segregation errors result from expansion of the ER inherited by mitotic CTDNEP1 knockout cells, then inhibition of FA synthesis would additionally suppress formation of micronuclei. Small molecule inhibition of
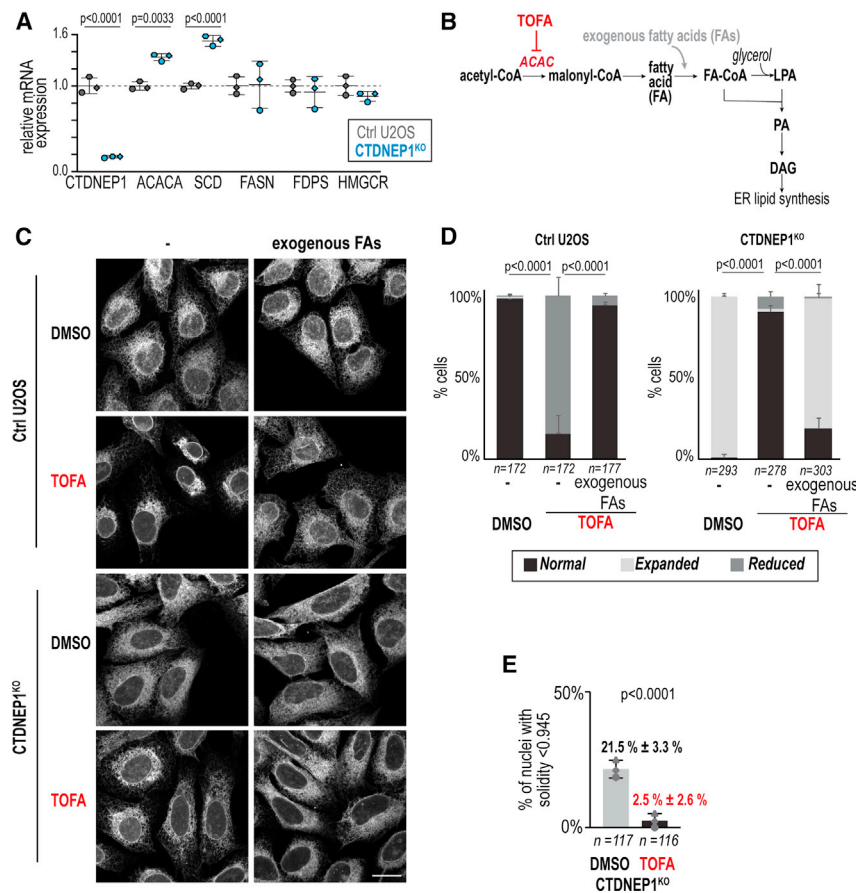
Figure 5. CTDNEP1 controls *de novo* FA synthesis to limit ER membrane biogenesis

(A) qRT-PCR of indicated cells for genes indicated, shown as fold change in expression relative to mean control values.

(B) Schematic representing target for inhibition by TOFA bypassed by addition of exogenous FAs.

(C) Max projections of confocal images in indicated cell lines under indicated conditions. Scale bar, 20 μm.

(D) Plot of incidences of indicated phenotypes.

(E) Incidence of nuclei with solidity <1 SD from mean solidity of control U2OS cells per indicated condition. For all: p value, unpaired t (A), χ^2 (D), or Fisher's exact (E) tests. 3 experimental repeats and means ± SDs shown. See also Figures S5 and S6.

fusion of permeabilized pronuclear membranes in *C. elegans* embryos) (Bahmanyar et al., 2014; Barger et al., 2021; Dey and Baum, 2021; Dey et al., 2020; Makarova et al., 2016; Webster et al., 2009). Thus, restricting ER membrane biogenesis in interphase may be a crucial feature that helps prevent mitotic errors in animal cells that have evolved to undergo open mitosis.

Our data showing that the frequency of lagging chromosomes and formation of micronuclei upon transient spindle disassembly is increased under conditions when ER membranes are expanded suggests that dampened chromosome dynamics resulting from the increase in the effective viscosity of the mitotic cytoplasm impedes the correction of merotelic orientations (Figure 7) (Cimini et al., 2003). In agreement with this idea, mitotic chromosomes induced to persist in the peripheral ER are more likely to missegregate (Ferrandiz et al., 2021). Merotelic attachments go unnoticed by the SAC (Cimini, 2008) and are a major source of aneuploidy in cancer cells (Cimini, 2008; Cimini et al., 2002, 2001). In a merotelically oriented kinetochore, loss of attachment from one pole can allow the chromosome to biorient—forces from MTs on the attached kinetochore promote the chromosome to move so that the unattached kinetochore faces the proper spindle pole (Cimini, 2008; Cimini et al., 2003) (Figure 7). We propose that slower chromosome mobilities resulting from the increase in viscosity of the surrounding thickened ER network impedes error correction by slowing chromosome biorientation, resulting in re-attachment of the kinetochore to the incorrect pole (Figure 7).
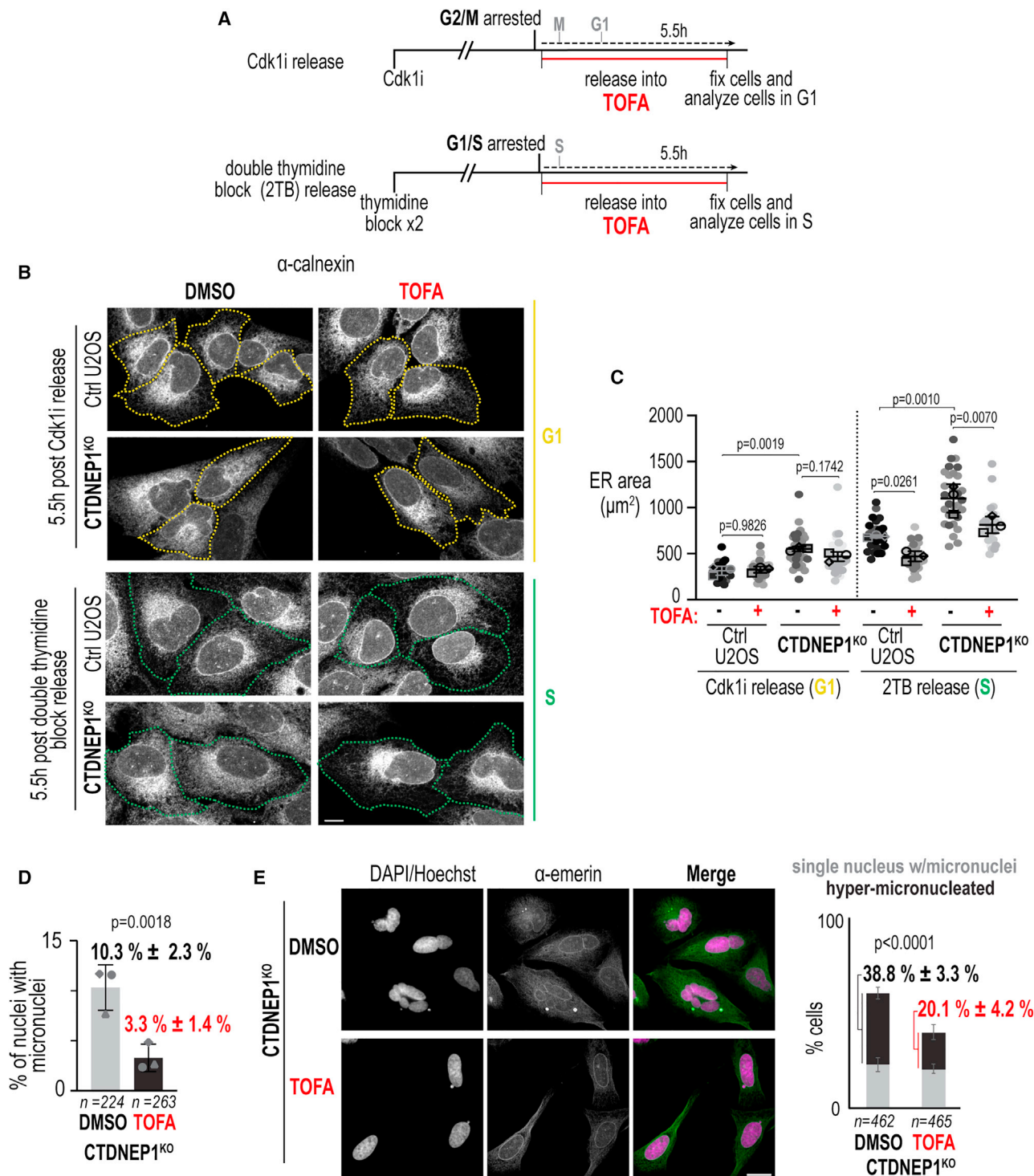
Our data suggest that regulation of the phosphorylation state of lipin 1 in interphase as determined by CTDNEP1 controls the flux of *de novo* FAs toward glycerophospholipid synthesis to restrict ER size prior to cell entry into mitosis. Although we cannot exclude the possibility that lipin 1 may have a more local role in PA to DAG conversion to control ER lipid synthesis, its overall PAP activity is partially reduced in CTDNEP1-deleted cells. This together with the fact that there is less lipin 1 in the nucleus of CTDNEP1-deleted cells in early interphase suggests that ER expansion may result from the increased expression in

ACAC with TOFA in CTDNEP1 knockout cells suppressed the increased incidence of micronuclei (Figure 6D) as well as the hyper-micronucleation phenotype that occurs after transient spindle disassembly (Figure 6E). Thus, limiting the production of ER membranes during interphase through downregulation of *de novo* FA synthesis by CTDNEP1 control of lipin is necessary for mitotic fidelity.
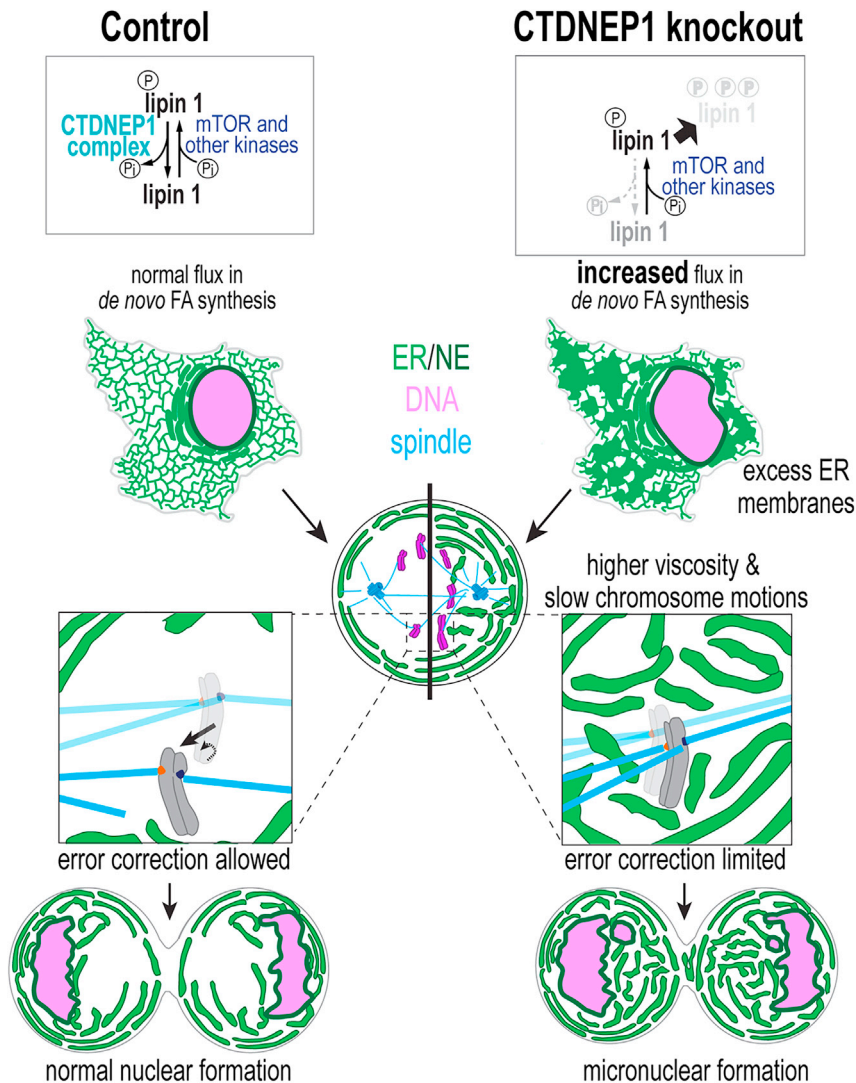
DISCUSSION

Our data indicate that ER membranes inherited from interphase dictate the biophysical properties of the cytoplasm of mitotic cells and that limiting their production protects against errors in chromosome segregation (Figure 7). CTDNEP1's role in dephosphorylation of lipin 1 in interphase prevents errors in mitosis by restricting excessive ER membrane proliferation, which allows the timely clearance of membranes from the spindle region in prometaphase. The cytoplasm is shared by membrane-bound organelles and mitotic chromosomes upon NE breakdown in animal cells, necessitating ER membrane reorganization away from the spindle region (Liu and Pellman, 2020). In human cells, the breakdown of the NE and the assembly of the mitotic spindle occurs simultaneously; in lower eukaryotes, these events are temporally uncoupled, which provides an explanation for why excess ER membranes do not invade mitotic chromosomes during prometaphase in those systems (e.g., the metaphase plate forms prior to completion of retraction and

Figure 6. Inhibition of FA synthesis in interphase suppresses the expanded ER phenotype of CTDNEP1 knockout cells and the increased incidence of micronuclei

(A) Schematic of experimental setup.

(B) Max projections of confocal images of cells treated as indicated. Borders: cells in distinct cell cycle stages as determined by markers (see Figure S7A). Scale bar, 10 μm.

(C) Plots of ER area in cells in specified stages treated as indicated. p values, one-way repeated measures ANOVA with Šidák's test.

(D) Plot of incidence of micronuclei in cells treated as indicated. p values, Fisher's exact test.

(E) Confocal images of indicated cell lines per condition following nocodazole washout. Scale bar, 20 μm. Plot: incidence of specified phenotypes. p value, χ^2 test. For all: 3 experimental repeats; means ± SDs shown. See also Figure S7.

Figure 7. Cell-cycle-regulated ER membrane biogenesis by CTDNEP1 dephosphorylation of lipin 1 allows chromosome movements necessary for biorientation

When CTDNEP1 is absent, phosphorylation of lipin 1 by mTOR and other kinases prevails and leads to decreased lipin 1 stability and an increased flux in *de novo* FA synthesis toward ER membrane biogenesis in interphase. Excess ER membranes inherited by mitotic cells contribute to higher cytoplasmic viscosity and dampened chromosome motions. The lack of chromosome motions limits mitotic error correction, leading to micronuclei formation.

in mitotic cells does not depend on CTDNEP1. CTDNEP1 requires its binding partner NEP1R1 to dephosphorylate lipin 1 (Han et al., 2012) and so one possibility is that this association, which could involve other factors (Jacquemyn et al., 2021; Papagiannidis et al., 2021), is regulated in a cell-cycle-dependent manner. In other systems, it has been shown that lipin is a target of Cdk1 (Makarova et al., 2016) and so it is also possible that Cdk1 activity in mitosis overrides the phosphatase activity of CTDNEP1 toward lipin 1. Other phosphatases are known to dephosphorylate lipin (Kok et al., 2014; Okuno et al., 2019) and so CTDNEP1 may target phosphosites on lipin 1 specific to regulation of ER lipid synthesis in interphase. Human lipin 1 has ~30 predicted phosphorylation sites (Boroda et al., 2017) and so future work will be required to understand the relationship between CTDNEP1 targeting of lipin 1 phospho-sites and the regulation of FA flux toward ER membrane biogenesis.

SREBP1 target genes ACACA and SCD, which are downregulated by nuclear-localized lipin 1 through an unknown mechanism (Peterson et al., 2011). We suggest that lipin 1 activity may well exceed the amount of PA in ER membranes under normal conditions allowing for lipin 1 to maintain low PA levels in ER/NE membranes and at the same time be a target of regulation in response to different signals. Future work is required to understand how the lack of dephosphorylation of lipin 1 by CTDNEP1 affects other aspects of its regulation to control ER membrane biogenesis (Bahmanyar and Schlieker, 2020; Gu et al., 2021; Kwiatek and Carman, 2020; Zhang and Reue, 2017; Zhang et al., 2014).

Prior work *in vitro* suggested that CTDNEP1 dephosphorylates a site on lipin 1 later confirmed to be targeted by mTOR (Wu et al., 2011). Work in budding yeast showed the dephosphorylation of Pah1 upon inhibition of Tor requires the presence of the Nem1/Spo7 complex (Dubots et al., 2014). We demonstrate that human CTDNEP1 counteracts phosphorylation of lipin 1 by mTOR to establish a dephosphorylated pool of lipin 1 in early interphase. We also show that the hyperphosphorylated lipin 1 species

The fact that loss of human CTDNEP1 contributes to chromosome instability through dysregulation of lipid metabolism is highly relevant to the fact that Group 3/4 medulloblastomas with high levels of genome instability frequently carry truncation mutations in CTDNEP1 (Jones et al., 2012; Northcott et al., 2012). Micronuclei occur frequently in cancer, and their membranes are prone to rupture, causing cancer-relevant chromosome rearrangements and activation of proinflammatory pathways (Hatch et al., 2013; Liu and Pellman, 2020; Ly and Cleveland, 2017; Mackenzie et al., 2017; Zhang et al., 2013). Increased *de novo* FA synthesis is also a hallmark of many cancers; however, why this is an advantage to tumor cells is not fully understood (Currie et al., 2013). Our data link increased FA synthesis to formation of micronuclei and define the mechanistic relationship between these processes. This work additionally suggests that aneuploidy in the context of oncogenic mTOR signaling may be mediated by misregulated lipid biosynthesis (Lamming and Sabatini, 2013). Together, these findings suggest that the use of inhibitors of enzymes in the *de novo* lipid synthesis pathway may be a potential therapeutic strategy in cancers

Developmental Cell
Article

CellPress

with chromosomal instability. Uncovering the significance of CTDNEP1 regulation of ER lipid synthesis in the context of chromosomal instability in cancer will be an exciting and important avenue of future research.

Limitations of this study

The mechanism by which CTDNEP1-lipin 1 limit FA synthesis to restrict ER membrane biogenesis in early interphase remains unclear. Previous work showed that the nuclear translocation of lipin 1 upon inhibition of mTOR inhibits SREBP1 target gene expression (Peterson et al., 2011). We show that CTDNEP1 promotes nuclear translocation of lipin 1 upon mTOR inhibition (Figure 4B) and in the absence of CTDNEP1 SREBP1 target genes are modestly elevated (Figure 5A). Furthermore, although lipin 1 is mainly cytoplasmic in control and CTDNEP1 knockout cells under steady state conditions (Figure 4B), there are fewer CTDNEP1 knockout cells in early interphase with nuclear-localized lipin 1 (Figure S7E). Together, our results suggest that CTDNEP1 dephosphorylation of a pool of lipin 1 ensures that lipid synthesis is not aberrantly upregulated in early interphase to cause overproliferation of ER membranes; however, the mechanisms for how phospho-regulation of lipin 1 controls its nuclear localization and how nuclear lipin 1 controls gene transcription are not fully understood. Therefore, how lipin 1 regulation by CTDNEP1 is mechanistically related to its nuclear versus cytoplasmic localization to in turn regulate FA synthesis remains unclear.

STAR★METHODS

Detailed methods are provided in the online version of this paper and include the following:

- KEY RESOURCES TABLE
- RESOURCE AVAILABILITY
  - Lead contact
  - Materials availability
  - Data and code availability
- EXPERIMENTAL MODEL AND SUBJECT DETAILS
  - Mammalian cell lines
  - CRISPR/Cas9 genome editing
  - Stable cell line generation
- METHOD DETAILS
  - Transfection and RNAi
  - Plasmid generation
  - Lipidomics
  - Measurement of lipin PAP activity
  - ^{14}C acetate labeling and lipid extraction
  - FA supplementation
  - Mitotic and micronuclei enrichment and drug treatments
  - Quantitative real-time PCR
  - Immunofluorescence
  - Immunoblot
- LIVE CELL IMAGING
  - Cytoplasmic viscosity measurements
  - Microscopy
  - Flow cytometry
  - Image analysis
- QUANTIFICATION AND STATISTICAL ANALYSIS

AUTHOR CONTRIBUTIONS

H.M. generated the knockout and fluorescent cell lines and performed most imaging experiments and lipidomic data analysis, J.W.C.R. generated stable cell lines and performed biochemistry experiments related to phosphorylation of lipin 1, T.V. performed lipin localization experiments, M.I.A.-D. (supervised by D.J.N.) performed magnetic tweezer and chromosome mobility experiments, and M.E.G. (supervised by T.E.H.) performed radiolabeling and PAP activity assays. H.M. and S.B. wrote the manuscript with input from other authors. S.B. supervised the project.

DECLARATION OF INTERESTS

The authors declare no competing interests.

INCLUSION AND DIVERSITY

One or more of the authors of this paper self-identifies as an underrepresented ethnic minority in science. One or more of the authors of this paper self-identifies as a member of the LGBTQ+ community.

REFERENCES

Bahmanyar, S., Biggs, R., Schuh, A.L., Desai, A., Müller-Reichert, T., Audhya, A., Dixon, J.E., and Oegema, K. (2014). Spatial control of phospholipid flux restricts endoplasmic reticulum sheet formation to allow nuclear envelope breakdown. Genes Dev 28, 121–126.

Bahmanyar, S., and Schlieker, C. (2020). Lipid and protein dynamics that shape nuclear envelope identity. Mol. Biol. Cell 31, 1315–1323.

Barger, S.R., Penfield, L., and Bahmanyar, S. (2021). Coupling lipid synthesis with nuclear envelope remodeling. Trends Biochem. Sci. https://doi.org/10.1016/j.tibs.2021.08.009.

Baumann, O., and Walz, B. (2001). Endoplasmic reticulum of animal cells and its organization into structural and functional domains. Int. Rev. Cytol. 205, 149–214.

Bertolio, R., Napoletano, F., Mano, M., Maurer-Stroh, S., Fantuz, M., Zannini, A., Bicciato, S., Sorrentino, G., and Del Sal, G. (2019). Sterol regulatory element binding protein 1 couples mechanical cues and lipid metabolism. Nat. Commun. 10, 1326.

Boroda, S., Takkellapati, S., Lawrence, R.T., Entwisle, S.W., Pearson, J.M., Granade, M.E., Mullins, G.R., Eaton, J.M., Villén, J., and Harris, T.E. (2017). The phosphatidic acid-binding, polybasic domain is responsible for the differences in the phosphoregulation of lipins 1 and 3. J. Biol. Chem. 292, 20481–20493.

CellPress

Developmental Cell
Article

Brinkman, E.K., Chen, T., Amendola, M., and van Steensel, B. (2014). Easy quantitative assessment of genome editing by sequence trace decomposition. Nucleic Acids Res *42*, e168.

Brohée, L., Demine, S., Willems, J., Arnould, T., Colige, A.C., and Deroanne, C.F. (2015). Lipin-1 regulates cancer cell phenotype and is a potential target to potentiate rapamycin treatment. Oncotarget *6*, 11264–11280.

Cecchini, M.J., Amiri, M., and Dick, F.A. (2012). Analysis of cell cycle position in mammalian cells. J. Vis. Exp. *59*, 3491.

Champion, L., Linder, M.I., and Kutay, U. (2017). Cellular reorganization during mitotic entry. Trends Cell Biol *27*, 26–41.

Champion, L., Pawar, S., Luithle, N., Ungricht, R., and Kutay, U. (2019). Dissociation of membrane-chromatin contacts is required for proper chromosome segregation in mitosis. Mol. Biol. Cell *30*, 427–440.

Cimini, D. (2008). Merotelic kinetochore orientation, aneuploidy, and cancer. Biochim. Biophys. Acta *1786*, 32–40.

Cimini, D., Fioravanti, D., Salmon, E.D., and Degrassi, F. (2002). Merotelic kinetochore orientation versus chromosome mono-orientation in the origin of lagging chromosomes in human primary cells. J. Cell Sci. *115*, 507–515.

Cimini, D., Howell, B., Maddox, P., Khodjakov, A., Degrassi, F., and Salmon, E.D. (2001). Merotelic kinetochore orientation is a major mechanism of aneuploidy in mitotic mammalian tissue cells. J. Cell Biol. *153*, 517–527.

Cimini, D., Moree, B., Canman, J.C., and Salmon, E.D. (2003). Merotelic kinetochore orientation occurs frequently during early mitosis in mammalian tissue cells and error correction is achieved by two different mechanisms. J. Cell Sci. *116*, 4213–4225.

Currie, E., Schulze, A., Zechner, R., Walther, T.C., and Farese, R.V., Jr. (2013). Cellular fatty acid metabolism and cancer. Cell Metab *18*, 153–161.

Dey, G., and Baum, B. (2021). Nuclear envelope remodelling during mitosis. Curr. Opin. Cell Biol. *70*, 67–74.

Dey, G., Culley, S., Curran, S., Schmidt, U., Henriques, R., Kukulski, W., and Baum, B. (2020). Closed mitosis requires local disassembly of the nuclear envelope. Nature *585*, 119–123.

Donkor, J., Sariahmetoglu, M., Dewald, J., Brindley, D.N., and Reue, K. (2007). Three mammalian lipins act as phosphatidate phosphatases with distinct tissue expression patterns. J. Biol. Chem. *282*, 3450–3457.

Dubots, E., Cottier, S., Péli-Gulli, M.-P., Jaquenoud, M., Bontron, S., Schneiter, R., and De Virgilio, C. (2014). TORC1 regulates Pah1 phosphatidate phosphatase activity via the Nem1/Spo7 protein phosphatase complex. PLoS One *9*, e104194.

Eaton, J.M., Mullins, G.R., Brindley, D.N., and Harris, T.E. (2013). Phosphorylation of lipin 1 and charge on the phosphatidic acid head group control its phosphatidic acid phosphatase activity and membrane association. J. Biol. Chem. *288*, 9933–9945.

English, A.R., and Voeltz, G.K. (2013). Endoplasmic reticulum structure and interconnections with other organelles. Cold Spring Harb. Perspect. Biol. *5*, a013227.

Fagone, P., and Jackowski, S. (2009). Membrane phospholipid synthesis and endoplasmic reticulum function. J. Lipid Res. *50* (Suppl), S311–S316.

Ferrandiz, N., Downie, L., Starling, G.P., and Royle, S.J. (2021). Endomembranes promote chromosome missegregation by ensheathing misaligned chromosomes. bioRxiv. https://doi.org/10.1101/2021.04.23.441091.

Finck, B.N., Gropler, M.C., Chen, Z., Leone, T.C., Croce, M.A., Harris, T.E., Lawrence, J.C., Jr., and Kelly, D.P. (2006). Lipin 1 is an inducible amplifier of the hepatic PGC-1alpha/PPARalpha regulatory pathway. Cell Metab *4*, 199–210.

Fonseca, C.L., Malaby, H.L.H., Sepaniac, L.A., Martin, W., Byers, C., Czechanski, A., Messinger, D., Tang, M., Ohi, R., Reinholdt, L.G., and Stumpff, J. (2019). Mitotic chromosome alignment ensures mitotic fidelity by promoting interchromosomal compaction during anaphase. J. Cell Biol. *218*, 1148–1163.

Friedman, J.R., and Voeltz, G.K. (2011). The ER in 3D: a multifunctional dynamic membrane network. Trends Cell Biol *21*, 709–717.

Grimsey, N., Han, G.-S., O'Hara, L., Rochford, J.J., Carman, G.M., and Siniossoglou, S. (2008). Temporal and spatial regulation of the phosphatidate phosphatases lipin 1 and 2. J. Biol. Chem. *283*, 29166–29174.

Gu, W., Gao, S., Wang, H., Fleming, K.D., Hoffmann, R.M., Yang, J.W., Patel, N.M., Choi, Y.M., Burke, J.E., Reue, K., and Airola, M.V. (2021). The middle lipin domain adopts a membrane-binding dimeric protein fold. Nat. Commun. *12*, 4718.

Habenicht, A.J., Glomset, J.A., Goerig, M., Gronwald, R., Grulich, J., Loth, U., and Schettler, G. (1985). Cell cycle-dependent changes in arachidonic acid and glycerol metabolism in Swiss 3T3 cells stimulated by platelet-derived growth factor. J. Biol. Chem. *260*, 1370–1373.

Han, G.-C., and Carman, G.M. (2004). Assaying lipid phosphate phosphatase activities. In Signal Transduction Protocols Methods in Molecular Biology, R.C. Dickson and G.M.D. Mendenhall, eds. (Humana Press), pp. 209–216.

Han, S., Bahmanyar, S., Zhang, P., Grishin, N., Oegema, K., Crooke, R., Graham, M., Reue, K., Dixon, J.E., and Goodman, J.M. (2012). Nuclear envelope phosphatase 1-regulatory subunit 1 (formerly TMEM188) is the metazoan Spo7p ortholog and functions in the lipin activation pathway. J. Biol. Chem. *287*, 3123–3137.

Harris, T.E., and Finck, B.N. (2011). Dual function lipin proteins and glycerolipid metabolism. Trends Endocrinol. Metab. *22*, 226–233.

Hatch, E.M., Fischer, A.H., Deerinck, T.J., and Hetzer, M.W. (2013). Catastrophic nuclear envelope collapse in cancer cell micronuclei. Cell *154*, 47–60.

Huang, L.-K., and Wang, M.-J.J. (1995). Image thresholding by minimizing the measures of fuzziness. Pattern Recognit *28*, 41–51.

Jackowski, S. (1994). Coordination of membrane phospholipid synthesis with the cell cycle. J. Biol. Chem. *269*, 3858–3867.

Jacquemyn, J., Foroozandeh, J., Vints, K., Swerts, J., Verstreken, P., Gounko, N.V., Gallego, S.F., and Goodchild, R. (2021). Torsin and NEP1R1-CTDNEP1 phosphatase affect interphase nuclear pore complex insertion by lipid-dependent and lipid-independent mechanisms. EMBO J *40*, e106914.

Jones, D.T., Jäger, N., Kool, M., Zichner, T., Hutter, B., Sultan, M., Cho, Y.J., Pugh, T.J., Hovestadt, V., Stütz, A.M., et al. (2012). Dissecting the genomic complexity underlying medulloblastoma. Nature *488*, 100–105.

Kim, Y., Gentry, M.S., Harris, T.E., Wiley, S.E., Lawrence, J.C., Jr., and Dixon, J.E. (2007). A conserved phosphatase cascade that regulates nuclear membrane biogenesis. Proc. Natl. Acad. Sci. USA *104*, 6596–6601.

Kok, B.P.C., Skene-Arnold, T.D., Ling, J., Benesch, M.G.K., Dewald, J., Harris, T.E., Holmes, C.F.B., and Brindley, D.N. (2014). Conserved residues in the N terminus of lipin-1 are required for binding to protein phosphatase-1c, nuclear translocation, and phosphatidate phosphatase activity. J. Biol. Chem. *289*, 10876–10886.

Kollmannsberger, P., and Fabry, B. (2007). High-force magnetic tweezers with force feedback for biological applications. Rev. Sci. Instrum. *78*, 114301.

Kumar, D., Golchoubian, B., Belevich, I., Jokitalo, E., and Schlaitz, A.-L. (2019). REEP3 and REEP4 determine the tubular morphology of the endoplasmic reticulum during mitosis. Mol. Biol. Cell *30*, 1377–1389.

Kwiatek, J.M., and Carman, G.M. (2020). Yeast phosphatidic acid phosphatase Pah1 hops and scoots along the membrane phospholipid bilayer. J. Lipid Res. *61*, 1232–1243.

Lamming, D.W., and Sabatini, D.M. (2013). A Central role for mTOR in lipid homeostasis. Cell Metab *18*, 465–469.

Liebergall, S.R., Angdisen, J., Chan, S.H., Chang, Y., Osborne, T.F., Koeppel, A.F., Turner, S.D., and Schulman, I.G. (2020). Inflammation triggers liver X receptor-dependent lipogenesis. Mol. Cell. Biol. *40*, e00364.

Liu, S., Kwon, M., Mannino, M., Yang, N., Renda, F., Khodjakov, A., and Pellman, D. (2018). Nuclear envelope assembly defects link mitotic errors to chromothripsis. Nature *561*, 551–555.

Liu, S., and Pellman, D. (2020). The coordination of nuclear envelope assembly and chromosome segregation in metazoans. Nucleus *11*, 35–52.

Lord, S.J., Velle, K.B., Mullins, R.D., and Fritz-Laylin, L.K. (2020). SuperPlots: communicating reproducibility and variability in cell biology. J. Cell Biol. *219*, e202001064.

Developmental Cell
Article

CellPress

Lu, L., Ladinsky, M.S., and Kirchhausen, T. (2011). Formation of the postmitotic nuclear envelope from extended ER cisternae precedes nuclear pore assembly. J. Cell Biol. *194*, 425–440.

Luithle, N., de Bos, J.U., Hovius, R., Maslennikova, D., Lewis, R.T., Ungricht, R., Fierz, B., and Kutay, U. (2020). Torsin ATPases influence chromatin interaction of the Torsin regulator LAP1. Elife *9*, e63614.

Ly, P., and Cleveland, D.W. (2017). Rebuilding chromosomes After catastrophe: emerging mechanisms of chromothripsis. Trends Cell Biol *27*, 917–930.

Mackenzie, K.J., Carroll, P., Martin, C.-A., Murina, O., Fluteau, A., Simpson, D.J., Olova, N., Sutcliffe, H., Rainger, J.K., Leitch, A., et al. (2017). cGAS surveillance of micronuclei links genome instability to innate immunity. Nature *548*, 461–465.

Makarova, M., Gu, Y., Chen, J.-S., Beckley, J.R., Gould, K.L., and Oliferenko, S. (2016). Temporal regulation of lipin activity diverged to account for differences in mitotic programs. Curr. Biol. *26*, 237–243.

Mall, M., Walter, T., Gorjánácz, M., Davidson, I.F., Nga Ly-Hartig, T.B., Ellenberg, J., and Mattaj, I.W. (2012). Mitotic lamin disassembly is triggered by lipid-mediated signaling. J. Cell Biol. *198*, 981–990.

Matsudaira, T., Mukai, K., Noguchi, T., Hasegawa, J., Hatta, T., Iemura, S.-I., Natsume, T., Miyamura, N., Nishina, H., Nakayama, J., et al. (2017). Endosomal phosphatidylserine is critical for the YAP signalling pathway in proliferating cells. Nat. Commun. *8*, 1246.

McCune, S.A., and Harris, R.A. (1979). Mechanism responsible for 5-(tetradecyloxy)-2-furoic acid inhibition of hepatic lipogenesis. J. Biol. Chem. *254*, 10095–10101.

Nabokina, S.M., Inoue, K., Subramanian, V.S., Valle, J.E., Yuasa, H., and Said, H.M. (2014). Molecular identification and functional characterization of the human colonic thiamine pyrophosphate transporter. J. Biol. Chem. *289*, 4405–4416.

Neuhaus, J., Schwalenberg, T., Horn, L.-C., Alexander, H., and Stolzenburg, J.-U. (2011). New aspects in the differential diagnosis and therapy of bladder pain syndrome/interstitial cystitis. Adv. Urol. *2011*, 639479.

Northcott, P.A., Jones, D.T., Kool, M., Robinson, G.W., Gilbertson, R.J., Cho, Y.-J., Pomeroy, S.L., Korshunov, A., Lichter, P., Taylor, M.D., and Pfister, S.M. (2012). Medulloblastomics: the end of the beginning. Nat. Rev. Cancer *12*, 818–834.

Odle, R.I., Walker, S.A., Oxley, D., Kidger, A.M., Balmanno, K., Gilley, R., Okkenhaug, H., Florey, O., Ktistakis, N.T., and Cook, S.J. (2020). An mTORC1-to-CDK1 switch maintains autophagy suppression during mitosis. Mol. Cell *77*, 228–240.e7.

O'Hara, L., Han, G.-S., Peak-Chew, S., Grimsey, N., Carman, G.M., and Siniossoglou, S. (2006). Control of phospholipid synthesis by phosphorylation of the yeast lipin Pah1p/Smp2p Mg2+-dependent phosphatidate phosphatase. J. Biol. Chem. *281*, 34537–34548.

Okuno, H., Okuzono, H., Hayase, A., Kumagai, F., Tanii, S., Hino, N., Okada, Y., Tachibana, K., Doi, T., and Ishimoto, K. (2019). Lipin-1 is a novel substrate of protein phosphatase PGAM5. Biochem. Biophys. Res. Commun. *509*, 886–891.

Papagiannidis, D., Bircham, P.W., Lüchtenborg, C., Pajonk, O., Ruffini, G., Brügger, B., and Schuck, S. (2021). ICE2 promotes ER membrane biogenesis in yeast by inhibiting the conserved lipin phosphatase complex. EMBO J. e107958. https://doi.org/10.15252/embj.2021107958.

Péterfy, M., Phan, J., and Reue, K. (2005). Alternatively spliced lipin isoforms exhibit distinct expression pattern, subcellular localization, and role in adipogenesis. J. Biol. Chem. *280*, 32883–32889.

Peterson, T.R., SenGupta, S.S., Harris, T.E., Carmack, A.E., Kang, S.A., Balderas, E., Guertin, D.A., Madden, K.L., Carpenter, A.E., Finck, B.N., and Sabatini, D.M. (2011). mTOR complex 1 regulates lipin 1 localization to control the SREBP pathway. Cell *146*, 408–420.

Puhka, M., Joensuu, M., Vihinen, H., Belevich, I., and Jokitalo, E. (2012). Progressive sheet-to-tubule transformation is a general mechanism for endoplasmic reticulum partitioning in dividing mammalian cells. Mol. Biol. Cell *23*, 2424–2432.

Puhka, M., Vihinen, H., Joensuu, M., and Jokitalo, E. (2007). Endoplasmic reticulum remains continuous and undergoes sheet-to-tubule transformation during cell division in mammalian cells. J. Cell Biol. *179*, 895–909.

Ran, F.A., Hsu, P.D., Wright, J., Agarwala, V., Scott, D.A., and Zhang, F. (2013). Genome engineering using the CRISPR-Cas9 system. Nat. Protoc. *8*, 2281–2308.

Schindelin, J., Arganda-Carreras, I., Frise, E., Kaynig, V., Longair, M., Pietzsch, T., Preibisch, S., Rueden, C., Saalfeld, S., Schmid, B., et al. (2012). Fiji: an open-source platform for biological-image analysis. Nat. Methods *9*, 676–682.

Schlaitz, A.-L., Thompson, J., Wong, C.C., Yates, J.R., 3rd, and Heald, R. (2013). REEP3/4 ensure endoplasmic reticulum clearance from metaphase chromatin and proper nuclear envelope architecture. Dev. Cell *26*, 315–323.

Schweizer, N., Pawar, N., Weiss, M., and Maiato, H. (2015). An organelle-exclusion envelope assists mitosis and underlies distinct molecular crowding in the spindle region. J. Cell Biol. *210*, 695–704.

Seifried, A., Schultz, J., and Gohla, A. (2013). Human HAD phosphatases: structure, mechanism, and roles in health and disease. FEBS Journal *280*, 549–571.

Shimizu, K., Fukushima, H., Ogura, K., Lien, E.C., Nihira, N.T., Zhang, J., North, B.J., Guo, A., Nagashima, K., Nakagawa, T., et al. (2017). The SCFbeta-TRCP E3 ubiquitin ligase complex targets Lipin1 for ubiquitination and degradation to promote hepatic lipogenesis. Sci. Signal. *10*, eaah4117.

Siniossoglou, S., Santos-Rosa, H., Rappsilber, J., Mann, M., and Hurt, E. (1998). A novel complex of membrane proteins required for formation of a spherical nucleus. EMBO J. *17*, 6449–6464.

Smyth, J.T., Beg, A.M., Wu, S., Putney, J.W., Jr., and Rusan, N.M. (2012). Phosphoregulation of STIM1 leads to exclusion of the endoplasmic reticulum from the mitotic spindle. Curr. Biol. *22*, 1487–1493.

Sołtysik, K., Ohsaki, Y., Tatematsu, T., Cheng, J., Maeda, A., Morita, S.-Y., and Fujimoto, T. (2021). Nuclear lipid droplets form in the inner nuclear membrane in a seipin-independent manner. J. Cell Biol. *220*, e202005026.

Steigemann, P., Wurzenberger, C., Schmitz, M.H., Held, M., Guizetti, J., Maar, S., and Gerlich, D.W. (2009). Aurora B-mediated abscission checkpoint protects against tetraploidization. Cell *136*, 473–484.

Tange, Y., Hirata, A., and Niwa, O. (2002). An evolutionarily conserved fission yeast protein, Ned1, implicated in normal nuclear morphology and chromosome stability, interacts with Dis3, Pim1/RCC1 and an essential nucleoporin. J. Cell Sci. *115*, 4375–4385.

Thielicke, W. (2014). The flapping flight of birds: analysis and application. In Ocean Ecosystems (University of Groningen).

Thielicke, W., and Stamhuis, E.J. (2014). PIVlab – Towards user-friendly, affordable and accurate digital particle image velocimetry in MATLAB. J. Open Res. Software *2*, e30.

Thompson, S.L., and Compton, D.A. (2011). Chromosome missegregation in human cells arises through specific types of kinetochore-microtubule attachment errors. Proc. Natl. Acad. Sci. USA *108*, 17974–17978.

Turgay, Y., Champion, L., Balazs, C., Held, M., Toso, A., Gerlich, D.W., Meraldi, P., and Kutay, U. (2014). SUN proteins facilitate the removal of membranes from chromatin during nuclear envelope breakdown. J. Cell Biol. *204*, 1099–1109.

Vassilev, L.T. (2006). Cell cycle synchronization at the G2/M phase border by reversible inhibition of CDK1. Cell Cycle *5*, 2555–2556.

Wang, S., Romano, F.B., Field, C.M., Mitchison, T.J., and Rapoport, T.A. (2013). Multiple mechanisms determine ER network morphology during the cell cycle in Xenopus egg extracts. J. Cell Biol. *203*, 801–814.

Webster, M., Witkin, K.L., and Cohen-Fix, O. (2009). Sizing up the nucleus: nuclear shape, size and nuclear-envelope assembly. J. Cell Sci. *122*, 1477–1486.

Witkin, K.L., Chong, Y., Shao, S., Webster, M.T., Lahiri, S., Walters, A.D., Lee, B., Koh, J.L., Prinz, W.A., Andrews, B.J., and Cohen-Fix, O. (2012). The budding yeast nuclear envelope adjacent to the nucleolus serves as a membrane sink during mitotic delay. Curr. Biol. *22*, 1128–1133.

Wu, R., Garland, M., Dunaway-Mariano, D., and Allen, K.N. (2011). Homo sapiens dullard protein phosphatase shows a preference for the insulin-dependent phosphorylation site of lipin1. Biochemistry *50*, 3045–3047.

Zhang, C.-Z., Leibowitz, M.L., and Pellman, D. (2013). Chromothripsis and beyond: rapid genome evolution from complex chromosomal rearrangements. Genes Dev. *27*, 2513–2530.

Zhang, P., and Reue, K. (2017). Lipin proteins and glycerolipid metabolism: roles at the ER membrane and beyond. Biochim. Biophys. Acta Biomembr. *1859*, 1583–1595.

Zhang, P., Verity, M.A., and Reue, K. (2014). Lipin-1 regulates autophagy clearance and intersects with statin drug effects in skeletal muscle. Cell Metab. *20*, 267–279.

Developmental Cell
Article

CellPress

STAR★METHODS

KEY RESOURCES TABLE

REAGENT or RESOURCE	SOURCE	IDENTIFIER
Antibodies		
Rabbit α calnexin	Abcam	Cat#ab22595; RRID: AB_2069006
Rabbit α emerin	Proteintech	Cat#10351; RRID: AB_2100056
Mouse α tubulin DM1A	Millipore Sigma	Cat#05-829; RRID: AB_310035
Mouse α FLAG	Sigma	Cat#F3165; RRID: AB_259529
Rabbit α HA	Cell Signaling Technologies	Cat#3724; RRID: AB_1549585
Rhodamine RedX Donkey α mouse IgG	Jackson Immuno	Cat#715-295-150; RRID: AB_2340831
FITC Goat α mouse IgG	Jackson Immuno	Cat#115-095-146; RRID: AB_2338599
FITC Goat α rabbit IgG	Jackson Immuno	Cat#111-095-003; RRID: AB_2337972
FITC Donkey α Goat IgG	Jackson Immuno	Cat#705-095-147; RRID: AB_2340401
Rhodamine RedX goat α rabbit IgG	Jackson Immuno	Cat#111-295-003; RRID: AB_2338022
Alexa Fluor 488 Donkey α mouse IgG	Jackson Immuno	Cat#715-545-150; RRID: AB_2340846
Alexa Fluor 647 goat α mouse IgG	Jackson Immuno	Cat#115-605-003; RRID: AB_2338902
Alexa Fluor 647 donkey α rabbit IgG	Jackson Immuno	Cat#711-605-152; RRID: AB_2492288
Rabbit α lipin-1	Millipore Sigma	Cat#ABS400 (discontinued)
Rabbit α lipin-1	Proteintech	Cat# 27026-1-AP; RRID: AB_2880727
Rabbit α Phospho-p70 S6 Kinase (Thr389) (108D2)	Cell Signaling Technology	Cat#9234; RRID: AB_2269803
Rabbit α p70 S6 kinase	Cell Signaling Technology	Cat#9202; RRID: AB_331676
Rabbit α Phospho 4E-BP1 (Ser65)	Cell Signaling Technology	Cat#9451; RRID: AB_330947
Rabbit α 4E-BP1	Cell Signaling Technology	Cat#9452; RRID: AB_331692
Rabbit α NRF2	Abcam	Cat#ab62352; RRID: AB_944418
Goat α mouse IgG-HRP	Thermo Fisher	Cat#31430; RRID: AB_228307
Goat α rabbit IgG-HRP	Thermo Fisher	Cat#31460; RRID: AB_228341
Mouse α cyclin A2	Proteintech	Cat#66391; RRID: AB_2881767
Mouse α BrdU	Santa Cruz	Cat#sc-32323; RRID: AB_626766
Mouse α cyclin B1 (GNS1)	Santa Cruz	Cat#sc-245; RRID: AB_627338
Mouse α cyclin E1 (HE12)	Cell Signaling Technology	Cat#4129; RRID: AB_2071200
Chemicals, peptides, and recombinant proteins		
Torin 1	ApexBio	Cat#A8312
Cycloheximide	Cell Signaling	Cat#2112
MG132 z-Leu-Leu-Leu-Al	Fisher Scientific	Cat#AAJ63250LB0
Nocodazole	Sigma	Cat#M1404
RO-3306	EMD Millipore	Cat#217699
TOFA	Cayman Chemicals	Cat#10005263
NMS-P715	EMD Millipore	Cat#475949
SiR-DNA	Cytoskeleton, Inc.	Cat#CY-SC007
ER Tracker Green	Invitrogen	Cat#E34251
Puromycin HCl	Thermo Fisher	Cat#A1113803
G418	EMD Millipore	Cat#345810
Blasticidin	Sigma	Cat#R21001
Palmitic acid	Sigma	Cat#P0500
Oleic acid	Sigma	Cat#O1008
Linoleic acid	Sigma	Cat#L5900
1,2-C14-acetic acid sodium salt	Perkin-Elmer	Cat#NEC553
ProMag™ 3 Series - Streptavadin beads	Bangslabs	Cat#PMS3N
1,2-Dioleoyl-sn-glycerol	Avanti Polar Lipids	Cat#800811

(Continued on next page)

Continued

REAGENT or RESOURCE	SOURCE	IDENTIFIER
1,2-Dioleoyl-sn-glycero-3-phosphate	Avanti Polar Lipids	Cat#840875
Triton X-100	Sigma-Aldrich	Cat# T9284
[γ-^{32}P] ATP (6000 Ci/mmol, 150 mCi/mL)	Perkin-Elmer	Cat# NEG035C005MC
Escherichia coli DAG kinase, 1 mg/mL, 2 U/mg	Sigma-Aldrich	Cat# D3065
5'ethynyl-2'-deoxyuridine (EdU)	Lumiprobe	Cat#10540
Sulfo-Cyanine 5 Azide	Lumiprobe	Cat#A3330
Bromodeoxyuridine (BrdU)	BioLegend	Cat#423401
Sodium tetraborate decahydrate	Sigma	Cat#S9640
RNAse A	Sigma	Cat#AB12023-00100
Propidium Iodide	BioLegend	Cat#421301
Thymidine	Sigma	T1895
2' deoxycytidine	Sigma	D3897
Critical commercial assays		
Zymopure II plasmid Midi prep kit	Zymogen	Cat#D4200
Pierce BCA Protein Assay kit	Thermo Scientific	Cat#23225
Experimental models: Cell lines		
U2OS	Slack lab (Harvard Medical School)	N/A
RPE-1	Breslow lab (Yale University)	N/A
HEK293	Breslow lab (Yale University)	N/A
U2OS GFP-Sec61β	Rapoport lab (Harvard Medical School)	N/A
U2OS GFP-Sec61β H2B-mCherry	This study	N/A
U2OS CTDNEP1^{KO}	This study	N/A
U2OS CTDNEP1^{KO} CTDNEP1-HA^{stable}	This study	N/A
U2OS CTDNEP1^{KO} CTDNEP1-HA^{stable} PD (D67E D69T)	This study	N/A
Oligonucleotides		
siRNA targeting sequence: CTDNEP1 custom single siRNA FWD, no modifications: AGGCAGAUCCGCACGGUAA	Dharmacon	N/A
siRNA targeting sequence: Lipin 1 custom single siRNA, no modifications: GAAUGGAAUGCCAGCUGAA	(Brohée et al., 2015) (Sołtysik et al., 2021), Dharmacon	N/A
siRNA targeting sequence: CTDNEP1 SMARTpool siRNA	Dharmacon	Cat#M-017869-00-0005
siRNA targeting sequence: siGENOME Non-targeting siRNA Pool #2	Dharmacon	Cat#D-001206-14-05
Silencer Negative control siRNA #1	Invitrogen	Cat#AM4611
Silencer Select negative control siRNA #1	Life Technologies	Cat#4390843
qPCR primer: Hs GAPDH forward: GTCTCCTCTGACTTCAACAGCG	(Nabokina et al., 2014)	N/A
qPCR primer: Hs GAPDH reverse: ACCACCCTGTTGCTGTAGCCAA	(Nabokina et al., 2014)	N/A
qPCR primer: Hs CTDNEP1 forward: CATTTACCTTCTGCGGAGGC	This study	N/A
qPCR primer: Hs CTDNEP1 reverse: CACCTGGGCTAGCCGATTC	This study	N/A
qPCR primer: Hs ACACA forward: TCACACCTGAAGACCTTAAAGCC	(Shimizu et al., 2017)	N/A
qPCR primer: Hs ACACA reverse: AGCCCACACTGCTTGTACTG	(Shimizu et al., 2017)	N/A
qPCR primer: Hs FDPS forward: TGTGACCGGCAAAATTGGC	(Shimizu et al., 2017)	N/A

Developmental Cell
Article

CellPress

Continued

REAGENT or RESOURCE	SOURCE	IDENTIFIER
qPCR primer: Hs FDPS reverse: GCCCGTTGCAGACACTGAA	(Shimizu et al., 2017)	N/A
qPCR primer: Hs SCD forward: TCTAGCTCCTATACCACCACCA	(Shimizu et al., 2017)	N/A
qPCR primer: Hs SCD reverse: TCGTCTCCAACTTATCTCCTCC	(Shimizu et al., 2017)	N/A
qPCR primer: Hs HMGCR forward: GGACCCCTTTGCTTAGATGAAA	(Bertolio et al., 2019)	N/A
qPCR primer: Hs HMGCR reverse: CCACCAAGACCTATTGCTCTG	(Bertolio et al., 2019)	N/A
qPCR primer: Hs FASN forward: CATCCAGATAGGCCTCATAGA	(Bertolio et al., 2019)	N/A
qPCR primer: Hs FASN reverse: CTCCATGAAGTAGGAGTGGAA	(Bertolio et al., 2019)	N/A
qPCR primer: Hs 36B4 forward: AACATGCTCAACATCTCCCC	(Neuhaus et al., 2011)	N/A
qPCR primer: Hs 36B4 reverse: CCGACTCCTCCGACTCTTC	(Neuhaus et al., 2011)	N/A
Recombinant DNA		
pSPCas9(BB)-2A-Puro (PX459) v2.0	(Ran et al., 2013)	Cat#62988; RRID: Addgene_62988
pH2B_mCherry_IRES_puro2	(Steigemann et al., 2009)	Cat#21045; RRID: Addgene_21045
GFP-KDEL	This study	N/A
pRK5 FLAG-lipin1β (Mm)	(Peterson et al., 2011)	RRID: Addgene_32005
pRK5 FLAG-lipin1β 19xA	(Peterson et al., 2011)	RRID: Addgene_32007
pRK5 FLAG-lipin1β 19xA PAP dead (D712E, D714E)	This study	N/A
Human lipin 1β-GFP	(Sołtysik et al., 2021)	N/A
pcDNA CTDNEP1-HA	This study	N/A
pcDNA CTDNEP1 D67E-HA	This study	N/A
pcDNA CTDNEP1 D67ED69T-HA	This study	N/A
FLAG-CNEP1R1	This study	N/A
pMRX CTDNEP1 D67E-HA	This study	N/A
pMRX CTDNEP1 D67ED69T-HA	This study	N/A
pMRX_EGFP_Blast	H. Arai lab (University of Tokyo)	N/A
Software and algorithms		
FIJI	(Schindelin et al., 2012)	https://imagej.net/Fiji
GraphPad Prism 8/9	GraphPad Software	https://www.graphpad.com/scientific-software/prism/
MATLAB	MathWorks	https://www.mathworks.com/products/matlab.html
PIVlab	(Thielicke, 2014; Thielicke and Stamhuis, 2014)	https://www.mathworks.com/matlabcentral/fileexchan
FlowJo 10	FlowJo, LLC	https://www.flowjo.com/solutions/flowjo
Image Lab Software	Bio-Rad	https://www.bio-rad.com/en-us/product/image-lab-software
ImageJ Filename_Randomizer	Tiago Ferreira (EMBL)	https://imagej.nih.gov/ij/macros/Filename_Randomizer.txt

RESOURCE AVAILABILITY

Lead contact
Further information and requests for resources and reagents should be directed to and will be fulfilled by the Lead Contact, Shirin Bahmanyar (shirin.bahmanyar@yale.edu).

Materials availability
Unique materials generated in this study are available from the Lead Contact without restriction.

Data and code availability
- All original data reported in this paper will be shared by the Lead Contact upon request.
- All original code generated in this study is available from the Lead Contact upon request.
- Any additional information required to reanalyze the data reported in this paper is available from the lead contact upon request.

EXPERIMENTAL MODEL AND SUBJECT DETAILS

Mammalian cell lines
U2OS, HEK293, and RPE-1 cells and derived cell lines (see key resource table) were obtained from the source specified. U2OS Sec61β-GFP cells were obtained from the Rapoport lab. Cells were grown at 37°C in 5% CO_2 in DMEM low glucose (Gibco 11885; U2OS), DMEM high glucose (Gibco 11965), or DMEM:F12+HEPES (Gibco 113300) supplemented with 2 mM L-glutamine (Sigma 59202C; RPE-1), all supplemented with 10% heat inactivated FBS (F4135) and 1% antibiotic-antimycotic (Gibco 15240112) or 50 IU/ml penicillin/streptomycin (Gibco 15140). Cells were used for experiments before passage 30 (20 for RPE-1). Cells were tested for mycoplasma upon initial thaw and generation of new cell lines (Southern Biotech 13100-01), and untreated cells were continuously profiled for contamination by assessment of extranuclear DAPI/Hoechst 33258 staining.

CRISPR/Cas9 genome editing
All guide RNA sequences were designed using the online CRISPR tool http://crispr.mit.edu and reported no off-target matches. CTDNEP1^{KO}: ATGAAGTCAGGAGGCGTACC. The guide RNA sequences were synthesized as two oligos with BbsI overhangs and an additional guanidine base 5′ to the protospacer sequence, and the oligos were phosphorylated with calf alkaline intestine phosphatase (New England BioLabs #M0290) and annealed by heating to 95°C and cooling to room temperature. The annealed oligos were cloned into pSPCas9(BB)-2A-Puro (PX459) v2.0 (a gift from Feng Zhang, Addgene plasmid #62988; (Ran et al., 2013)) that had been digested with BbsI-HF (New England BioLabs #R3539). The vector was transfected into U2OS cells using Lipofectamine 2000 and selected with 3 μg/ml puromycin (Invitrogen) for 48 hours. The remaining cells were grown up and gDNA isolated from the bulk population using a QiaAmp DNA Mini kit (Qiagen 51304). Genotyping was performed by sequencing and screening for indels using TIDE deconvolution (https://www.deskgen.com/landing/tide.html; (Brinkman et al., 2014). Once indels were detected in the bulk population, the cells were plated at <100 cells/ml into 96 well plates and grown in antibiotic-free DMEM with 10% FBS for 2 weeks. Colonies were grown in 24-well plates until more than 10,000 cells could be harvested for gDNA sequencing and TIDE analysis to genotype for frameshift mutations. The CTDNEP1^{KO} clonal cell line used in experiments showed to have +1 insertions in >80% of alleles and 0% WT alleles as determined by TIDE deconvolution of sequencing data.

Stable cell line generation
To generate U2OS GFP-Sec61β H2B-mCherry, U2OS GFP-Sec61β were transfected with H2B-mCherry-IRES-puro2v2.0 (Steigemann et al., 2009) for 48 hours, then plated into 10 cm dishes at <100 cells/ml and selected with 0.5 μg/ml puromycin for 2 weeks. Colonies were trypsinized and picked with 1/8 in sterile cloning discs (Bel-Art F37847-0001) and grown to confluence in a T25 flask before imaging confirmation of marker expression.

U2OS CTDNEP1^{KO}+CTDNEP1-HA stable cell lines were generated by retroviral transduction, and bulk populations of cells were used for experiments. Retroviruses were generated by transfecting HEK293T cells with pCG-gag-pol, pCG-VSVG and either pMRX-CTDNEP1-HA or pMRX-CTDNEP1-D67ED69T-HA using Lipofectamine 2000. The retroviruses were used to transduce U2OS CTDNEP1^{KO} cells and placed under 7.5 μg/mL blasticidin selection for 2 weeks, then frozen and/or used for experiments. Cells were continuously cultured in 7.5 μg/mL blasticidin.

METHOD DETAILS

Transfection and RNAi
Most transfections were performed with Lipofectamine 2000 (Thermo Fisher Scientific 11668) in Opti-MEM (Gibco 31985) using a 1:2 ratio of DNA:lipofectamine with DNA concentrations ranging from 0.05-0.3 μg DNA per cm^2 of growth surface. Briefly, DNA and lipofectamine were added to 10 μl OptiMEM per cm^2 of growth surface in separate borosilicate glass tubes (Thermo Fisher Scientific STT-13100-S). After 5 minutes of incubation, DNA solution was added to lipofectamine solution. After 15 minutes, DNA:lipofectamine mix was added dropwise to cells plated 16-24 hrs prior to transfection in fresh antibiotic-free media (1 ml/9.6 cm^2 growth surface). Media was exchanged for antibiotic-free media after 6 hours. Cells were imaged or processed after 24-48 hours. To increase transfection efficiency, plasmids used for live imaging were purified using the Zymopure II Plasmid Midi Prep kit, including a 10 min final elution at 56°C and use of the Zymopure endotoxin removal columns. Unless listed as stably expressed, fluorescent markers were transiently transfected.

Transfections for lipin 1 overexpression were performed using PolyJet in vitro DNA transfection reagent (Signagen SL100688) using a 1:3 ratio of DNA:Polyjet using 0.1 μg DNA per cm^2 of growth surface. Protocol is identical to previous transfection protocol except for using 5 μl High glucose DMEM per cm^2 of growth surface for mixes and no incubation before mixing reagents.

For experiments involving phenotype rescue with transient FLAG-lipin 1β construct overexpression, GFP-KDEL was used as a co-transfection marker, and untransfected cells within the same experiment were used as a negative control for effects of lipin 1β overexpression.

RNAi was performed using Dharmafect 1 (Horizon Discovery T-2001) in Opti-MEM according to the manufacturer's protocol at the indicated concentrations and durations. RNAi knockdown efficiency was determined with qRT-PCR or immunoblot analysis. For CTDNEP1 knockdown, U2OS Sec61β/H2B-mCherry were treated with 40 nM CTDNEP1 custom single siRNA or Ambion Silencer negative control 1 for 48 hours; all others were treated with 20 nM CTDNEP1 siGENOME SMARTpool or control pool siRNA for 72 hours. For lipin 1 knockdown, cells were treated with 20 nM Silencer Select Control #1 siRNA (Ambion) or lipin 1 custom single siRNA for 72 hours.

For quantification of lipin 1 localization, endogenous lipin 1 was depleted with RNAi (Brohée et al., 2015); cells were then transfected with siRNA-resistant human lipin 1β-GFP (Sołtysik et al., 2021).

Plasmid generation
GFP-KDEL was modified from pDsRed2-ER (Clontech), which contains a signal peptide and ER retention sequence (KDEL), by PCR of GFP with AgeI and HindIII sites, digestion of the insert and pDsRed2 with AgeI/HindIII (NEB R0552, R3104), and ligation. CTDNEP1-HA was modified from CTDNEP1-v5-His (Han et al., 2012), and Quikchange Mutagenesis (Agilent) was used to make the D67E and D69T mutations. pRK5 FLAG-lipin 1β 19xA PAP dead was modified from pRK5 FLAG-lipin 1β 19xA using Quikchange Mutagenesis to make the following mutations: D712E, D714E. pMRX_CTDNEP1-HA_Blast was modified from pMRX_EGFP_Blast (Matsudaira et al., 2017).

Lipidomics
Early-passage cells were counted by hemocytometer, suspended in PBS at a concentration of 3x10^6 cells/ml, and flash frozen in liquid nitrogen. Triplicate samples were submitted for each condition, and corresponding triplicate samples were lysed and protein extracted and protein concentration determined by Pierce BCA assay. Sample processing and lipidomics were performed and obtained at Lipotype GmbH. Samples were spiked with lipid class internal standards, and lipids were extracted using chloroform-methanol extraction using a Hamilton Robotics STARlet. Samples were infused using an Advion Triversa Nanomate automated nano-flow electrospray ion source with positive and negative ion mode utilized. Mass spectra were acquired using a Thermo Scientific Q-Exactive hybrid quadruple/Orbitrap mass spectrometer in MS-only or MSMS mode. Lipid species were identified using LipotypeXplorer, and data was processed using Lipotype LIMS and LipotypeZoom. Lipid class pmols/μg protein was determined using protein concentration and sample volume analyzed from each replicate.

Measurement of lipin PAP activity
PAP activity was measured by release of phosphate from [^{32}P]PA using Triton X-100 micelles with cell lysates as previously reported (Boroda et al., 2017). Briefly, radiolabeled [^{32}P]PA substrate was prepared by phosphorylating 1,2-Dioleoyl-*sn*–glycerol with *E. coli* diacylglycerol kinase and [γ-^{32}P]ATP and purified by thin-layer chromatography as described by Han and Carman (Han and Carman, 2004). To prepare the micelles, Triton X-100 was mixed with buffer A (50 mM Tris-HCl, 10 mM 2-mercaptoethanol, pH 7.4) to a final concentration of 10 mM. Next, 1 μmol of unlabeled 1,2-Dioleoyl-*sn*–glycero-3-phosphate was dissolved in chloroform and mixed with [^{32}P]PA (3,000 cpm/nmol) in a glass tube, dried to a thin film under N2 gas, and resuspended with 1 mL of 10 mM Triton X-100. Lysates prepared from U2OS cells containing 10 μg of total protein, radioactive micelles, and buffer A were combined to a final volume of 100 μL, and the reactions were allowed to proceed for 20 min at 30 °C with gentle agitation and were terminated with the addition of 500 μL of acidified methanol (MeOH·0.1N HCl). The final concentrations for all reactions were as follows: 50 mM Tris-HCl, 10 mM 2-mercaptoethanol, and 0.2 mM PA. Free phosphate was extracted with the addition of 1 mL chloroform followed by 1 mL 1M MgCl$_2$. The organic extraction was vortexed and 500 μL of the aqueous phase was transferred to a scintillation vial to measure the removal of ^{32}P from PA by a scintillation counter. The measurement of PAP activity was determined by following the release of the radiolabeled phosphate from [^{32}P]PA. Total PAP activity was measured by including 0.5 mM MgCl$_2$. PAP activity for Mg^{2+}-independent enzymes was measured by instead including 1 mM EDTA. The activity from assays containing lysate was normalized to activity in assays without enzymes present. Mg^{2+}-dependent PAP activity was calculated by subtracting the mean Mg^{2+}-independent activity from the total PAP activity.

^{14}C acetate labeling and lipid extraction
U2OS cells were plated in 24 well plates at a density of 60,000 cells/well and cultured in low-glucose DMEM (Gibco, 11885-084) with 10% FBS (Gemini Bio-products, 900-108) and 1% antibiotic-antimycotic (Gibco, 15240-062). Cells were labeled with ^{14}C acetate and lipids extracted to determine acetate incorporation into neutral lipids (Liebergall et al., 2020). 16–18 hours after plating, cells were labeled with 500 μl fresh media containing 1 μCi/mL (19.23 μM) 1,2-^{14}C-acetate (Perkin-Elmer, NEC553) for 5 hours. Cells were then washed with PBS 2x on ice, lysed with 250 μL of 0.1% Triton X-100, 0.5 mM DTT, and a protease inhibitor cocktail (10 μg/mL leupeptin, 10 μg/mL pepstatin A, and 1 mM phenylmethylsulfonyl fluoride) in PBS, pH 7.2, and homogenized by pushing

through a 22G needle 6x. 200 μl of lysate was added to 500 μl 0.1 N HCl·methanol, then 250 μl chloroform was added. The extract was vortexed and incubated for 1-2 min at room temp. Another 250 μl of chloroform was added, followed by 250 μl of 0.2M NaCl. The extract was vortexed and centrifuged at 1000xg for 1 min. The aqueous phase was then aspirated, and 250 μl of the organic phase was used for quantification of ^{14}C by a Beckman-Coulter scintillation counter. To calibrate counts per minute per nmol ^{14}C-acetate, 250 μl media containing 1 μCi/ml ^{14}C acetate was counted. Remaining cell lysates were used for BCA protein quantification for normalizing to protein concentration. To account for background ^{14}C quantification, a control set of cells was treated with 10 μM 5-(tetradecyloxy)-2-furoic acid (TOFA) in DMSO 30 min before and during ^{14}C labeling, and these values were subtracted from final values and shown separately. Results were expressed as nmol^{14}C acetate incorporated into lipids per mg of protein.

FA supplementation

Cells were plated at a density of 200,000 cells/ml in 6 well plates. Stocks of oleic acid, linoleic acid, and palmitic acid were made in methanol and pipetted into a 50 ml conical vial, then dried with an ambient air stream. Pre-warmed DMEM containing 0.5% FA-free BSA (Sigma Cat#A8806) was added to a final concentration of 25 μM palmitic acid, 50 μM oleic acid, and 25 μM linoleic acid (100 μM total FA concentration; 1:2:1 ratio of palmitic:oleic:linoleic acid). The solution was incubated at 37°C for 30 min, then held to the bottom of a sonicating bath for 30 s, then incubated at 37°C for 10 min until solution was clear. FBS was added to a final concentration of 10% v/v. Cells were treated with DMEM with 10% FBS and 0.5% BSA alone or DMEM with 10% FBS 0.5% BSA, and 100 μM FAs with DMSO or 10 μM TOFA in DMSO for 24 hrs prior to immunofluorescence processing.

Mitotic and micronuclei enrichment and drug treatments

For mitotic shake off to enrich for M phase cells, cells were grown to at least 50% confluence in 75 cm^2 flasks. Cells were washed with PBS or antibiotic-free media to clear debris, then flasks were whacked repeatedly on all sides and tapped on the bottom surface with a reflex hammer (DR Instruments S72118) until at least 50% of mitotic cells were dislodged. The cell media was collected and centrifuged at 300xg for 5 min, then cells were additionally washed or plated.

For imaging intracellular ER membranes in prometaphase-metaphase cells, whole 75 cm^2 flasks of cells were transfected with GFP-KDEL and imaged 48 hours later after mitotic shake off and plating into 1 well of an ibidi 8-well imaging chamber per flask. Cells expressing GFP-KDEL in prometaphase up until metaphase (determined by DIC chromatin appearance) were imaged with 0.5 μm z stacks for 20 μm total z height.

For enrichment of cells at the G2-M phase transition by Cdk1 inhibition, cells were treated with 9 μM RO-3306 for 17-20 hours (Vassilev, 2006). On the microscope stage for live imaging of ER membrane (transiently-expressed GFP-KDEL) dynamics relative to chromosomes (transiently-expressed H2B-mCherry), media was exchanged for Fluorobrite DMEM with 10% FBS and 1 mM L-glutamine 7 times, then imaging was initiated within 5-10 min of the first wash. For RO-3306/MPS1i micronuclei enrichment, cells were treated with 9 μM RO-3306 (Calbiochem 217699) for 19 hours, then with 1 μM NMS-P715 (MPS1i; Calbiochem 475949) for 18 hours before processing for immunofluorescence (Liu et al., 2018). For release of G2/M cells into TOFA, cells were synchronized for 19 hours with 9 μM RO-3306 and then released (after 7 media washes) into media containing 10 μM TOFA or DMSO for 5.5 hours.

For micronuclei enrichment using nocodazole washout, cells at 50-80% confluence in 75 cm^2 flasks were washed with 37°C PBS to clear debris and then treated with 100 ng/ml nocodazole (Sigma M1404) in antibiotic-free media for 6 hours (Liu et al., 2018). Cells were subject to mitotic shake off without washing, then washed 3x with 37°C PBS. After the final wash, cells were plated onto acid-washed coverslips (coated with 1 μg/ml poly-D-lysine (Sigma P7886) for short-term washout) and incubated for 45 min-60 min (short-term) or 18-20 hours (long-term) before immunofluorescence processing. Cells treated with 10 μM TOFA or DMSO were treated during the 6 hour nocodazole treatment and during the 18 hour recovery period for 24 hours total treatment.

For synchronization of cells at the G1/S transition for immunofluorescence or detection of lipin 1phosphorylation state after 5.5h of release, cells were treated with 2 mM thymidine for 23 hours, then washed with media 3 times, then treated with 10 μM 2'-deoxycytidine for 8 hours. Cells were then treated with 2 mM thymidine for 16 hours followed by 3 media washes to release cells from G1/S, then incubated in media containing 10 μM 2'deoxycytidine. For release of G1/S cells into TOFA, cells were released into media containing 10 μM 2' deoxycytidine and 10 μM TOFA or DMSO for 5.5 hours. For immunoblot detection of G1/S-S enrichment, a cyclin E1 antibody was used.

For mitotic release in nocodazole-arrested cells to detect the phosphorylation state of lipin 1 upon mitotic exit, 2.0x10^6 cells plated in T75 flasks were treated with 2.5 mM thymidine (Sigma T1895) for 24 hrs. After 24 hrs, cells were released from thymidine and treated with 40 ng/ml nocodazole for 18 hrs. Cells were then subjected to mitotic shake off upon release from nocodazole and lysates were collected every 40 min.

When indicated, cells were treated with the following concentrations of drugs for the indicated times: Torin 1, 250 nM; MG132, 30 μM; Cycloheximide, 100 μg/ml; TOFA, 10 μM. Torin 1 treatment was for 4 hours unless otherwise indicated. Cells treated with cycloheximide were pre-treated with DMSO or Torin 1 for 2 hours prior to treatment with cycloheximide combined with either DMSO or Torin 1. TOFA treatment was for 24 hours (analysis of asynchronous cell ER or nuclear solidity), 48 hours (analysis of incidence of micronuclei), or other times as mentioned above.

Quantitative real-time PCR

RNA was harvested using the RNeasy Mini kit (Qiagen 74104) using the manufacturer's protocol, using Qiashredders (Qiagen 79654) for tissue homogenization and with additional RNase-free DNase (Qiagen 79254) treatment after the first RW1 wash and

subsequently adding another RW1 wash. RNA was eluted with RNAse-free water and diluted to 50 ng/μl. RNA was subject to reverse transcription using the iScript Reverse Transcription Supermix (Bio-Rad 1708840) with 400 ng RNA per reaction. The subsequent cDNA was diluted 1:5 for RT-qPCR. cDNA was analyzed for RT-qPCR using the iTaq universal SYBR Green Supermix (Bio-Rad 1725120). Cycle threshold values were analyzed using the ΔΔCt method. Values were normalized to expression of GAPDH (testing CTDNEP1 expression in U2OS/RPE-1 depleted of CTDNEP1 and CTDNEP1^{KO} U2OS; Nabokina et al., 2014) or 36B4 (testing expression of SREBP target genes and CTDNEP1 in CTDNEP1^{KO} U2OS cells; Neuhaus et al., 2011). SREBP target gene primer sequences were obtained from previous studies in human cells (Bertolio et al., 2019; Shimizu et al., 2017). Results are expressed as fold change in expression relative to mean of control values. Statistical testing was performed on ΔCt values.

Immunofluorescence
Cells were washed 2x with warm PBS and fixed in 4% paraformaldehyde (+0.1% glutaraldehyde for ER structure analyses) in PBS for 15 min, permeabilized in 0.5% Triton X-100 for 5 min, then washed 3 times with PBS and blocked in 3% BSA in PBS for 30 min. Samples were transferred to a humidity chamber and incubated with primary antibodies in 3% BSA in PBS for 1 hour at room temperature with rocking. Samples were washed with PBS 3 times for 5 min, then incubated with secondary antibodies in 3% BSA in PBS for 1 hour at room temperature in the dark with rocking. Samples were then washed with PBS 3 times for 5 min in the dark. For experiments visualizing nuclear structure and/or micronuclei, cells were additionally stained with 1 μg/ml Hoechst 33258 (Thermo Fisher Scientific H3569) in PBS for 1 min followed by one PBS wash. Coverslips were mounted with ProLong Gold Antifade reagent + DAPI (Thermo Fisher P36935) and sealed with clear nail polish. For samples treated with goat primary antibodies, 5% normal donkey serum (Sigma D9663) was used in place of 3% BSA.

For determination of interphase cell cycle staging, cells were treated with 20 μM 5-ethynyl-2'- deoxyuridine (EdU; Lumiprobe 10540) in media for 30 minutes before fixation. Between fixation and permeabilization, fixation was quenched with 100 mM Tris pH 7.5 for 5 minutes. After permeabilization and washing with PBS, coverslips were incubated for 30 minutes with freshly-prepared Cy5-azide mix consisting of 2 mM copper II sulfate pentahydrate (Sigma 209198), 8 μM sulfo-Cy5 azide (Lumiprobe), and 20 mg/ml freshly dissolved ascorbic acid (added last) in PBS. After Cy5-azide coupling, coverslips were washed briefly with PBS 2-3x, then washed for 5 minutes with PBS 3x. Immunofluorescence then proceeded as in the previous protocol starting with the blocking step.

When indicated, cells were fixed and stained to visualize kinetochore MTs (Thompson and Compton, 2011) by extracting in 100 mM PIPES, 1 mM MgCl₂, 1 mM CaCl₂, 0.5% Triton X-100, pH 6.8 for 4 min, then fixing in 1% glutaraldehyde in PBS for 10 min and quenched 2 times with 0.1% NaBH₄ in TBS for 10 min each. Cells were washed twice with 10 mM Tris, 150 mM NaCl, 10% BSA and then stained with tubulin antibody for 1.5 hours, washed with PBS, then stained with secondary antibody for 1 hour, washed with PBS, then mounted with ProLong Gold + DAPI.

Antibody concentrations used were: Rabbit anti-calnexin 1:1000; Mouse anti-Flag 1:1000; Rabbit anti-emerin 1:200; Mouse anti-α tubulin DM1A 1:1000; Mouse anti-cyclin A2 1:750; Goat anti-GFP 1:1000; all secondaries, 1:200-1:250.

Immunoblot
Lysis buffer used was: 0.1% Triton X-100, 50 mM NaF, 1mM EDTA, 1 mM EGTA, 10 mM Na₂HPO₄, 50 mM β-glycerophosphate, 1 tablet/50 ml cOmplete protease inhibitor cocktail, pH 7.4. Cell lysates were removed from growth surfaces by scraping with a rubber policeman after incubation in lysis buffer or by adding lysis buffer to cell pellets collected by trypsinization and centrifugation at 300xg for 5 min followed by 1-2 PBS washes. Lysates were homogenized by pushing through a 23G needle 30 times and then centrifuged at >20,000xg for 10 min at 4°C, then protein concentration was determined using the Pierce BCA Protein assay kit (Thermo Scientific 23225). 10-30 μg of whole cell lysates/lane were run on 8-15% polyacrylamide gels dependent on target size, and protein was wet transferred to 0.22 μm nitrocellulose. Ponceau S staining was used to visualize transfer efficiency, then washed with TBS or DI water; then, membranes were blocked in 5% nonfat dry milk or BSA in TBS for 1 hour. Membranes were then incubated with primary antibodies in 5% milk or BSA for 1-2 hours at room temperature or overnight at 4°C with rocking. Membranes were washed 3 times for 5 min in TBS-T, then incubated with anti-HRP secondary antibodies in 5% milk or BSA in TBS-T for 1 hour at room temperature with rocking. Membranes were washed 3 times for 5 min in TBS-T. Clarity or Clarity Max ECL reagent (Bio-Rad 1705060S, 1705062S) was used to visualize chemiluminescence, and images were taken with a Bio-Rad ChemiDoc or ChemiDoc XRS+ system. Exposure times of images used for analysis or presentation were maximum exposure before saturation of pixels around or within target bands.

Antibody concentrations used were: Mouse anti-α tubulin DM1A 1:5000; Mouse anti-FLAG 1:4000; Rabbit anti-HA 1:1000; Rabbit anti-lipin 1 1:1000; Rabbit anti-Phospho-p70 S6 Kinase (Thr389; 108D2) 1:1000; Rabbit anti-p70 S6 kinase 1:1000; Rabbit anti-Phospho 4E-BP1 (Ser65) 1:1000; Rabbit anti-4E-BP1 1:1000; mouse anti-cyclin B1, 1:1000; mouse anti-cyclin E1 1:1000, all secondaries 1:10000

LIVE CELL IMAGING

For live imaging, cells were plated in Willco Wells 35 mm dishes (Willco Wells HBST-3522), ibidi 2 well imaging chambers (ibidi 80287) with DIC lid (ibidi 80055); or ibidi 8 well imaging chambers (ibidi 80827). Samples were imaged in a CO2-, temperature-, and humidity-controlled Tokai Hit Stage Top Incubator. Objectives were also heated to 37°C. For CO2-controlled imaging, the imaging media used was Fluorobrite DMEM (Gibco A1896701) supplemented with 10% FBS. U2OS GFP-Sec61β/H2B-mCherry mitotic cells were imaged using a custom aluminum stage insert heated to 37°C with heating tape and temperature monitored using a Physitemp

thermistor (BAT7001H) and probe (IT-18), with objective heating and using 140 mM NaCl, 2.5 mM KCl, 1.8 mM CaCl$_2$, 1.0 mM MgCl$_2$, 20 mM HEPES, 15 mM glucose, pH 7.4 as the live cell imaging solution. When indicated, cells were treated with 1 μM SiR-DNA (Cytoskeleton, Inc. CY-SC007) for 1 hour prior to imaging and kept in SiR-DNA-containing live imaging media during imaging. When indicated, cells were treated with 1 μM ER Tracker Green (Invitrogen E34251) for 30 min and washed out prior to imaging, and cells were imaged for a maximum of 2 hours after treatment.

Cytoplasmic viscosity measurements

To prepare for cytoplasmic viscosity measurements, 2.75+/-0.219 μm diameter streptavidin-functionalized superparamagnetic beads (Bangslabs PMS3N) were incubated with 1 μM 647 fluorophore (Atto647N Biotin, Sigma 93606) for 2 hours at 4 C, shaking at 400 RPM. Cells were plated with beads during passaging and left to grow for 2-3 days until 75-80% confluent. Cells were passaged in this way for 3-4 cycles until visual inspection of cells shows approximately 40% of mitotic cells contain a single bead. Cells were grown in 35 mm Desag 263 glass-bottomed culture dish (0.17 mm thick glass black DeltaT, 04200417B, Bioptechs) to 75-80% confluency. Prior to experiments, cell medium was switched to an imaging medium (FluoroBrite DMEM, Gibco) supplemented with 10 mM HEPES and left to equilibrate for 10-20 minutes. Then a layer of 1 mL white mineral oil (VWR) was added on top of the imaging medium, and the dishes were mounted in a temperature control system and kept at 37 $^{\circ}$C (DeltaT Culture Dish System, Bioptechs). Only metaphase cells displaying proper chromosome alignment, no significant blebbing or morphological issues, and a high expression level of the expected tags, and having a single bead were selected for experiments.

The cylindrical magnetic tweezer core was made of ¼'' wide, 6'' long HyMu80 alloy (EFI Alloy 79, Ed Fagan Inc.) and sharpened at one end to a cone with a tip width of 5 μm. The solenoid frame was a steel cylinder 1'' wide, 3'' long, and has a hole for the core to fit through. The frame was held onto the core using 2 set screws. The solenoid was made using sheathed, 24-gauge copper wire (7588K77, McMaster-Carr) and wound 400 times. The solenoid and core were mounted on a micromanipulator (NMN-21, Narishige), which was mounted on a custom-built base using ThorLabs components. The solenoid was connected to a programmable power supply (PSP-603, GW Instek).

To analyze cytoplasmic viscosity measurements, we built a custom MATLAB pipeline. Briefly, we used featuretrack, an open-source MATLAB package by Maria Kilfoil, modified with a 3D Gaussian fit to localize the bead each frame and calculate displacement between successive frames. Once we found the full trajectory of the bead, we fit the velocity, bootstrapping using 50% of the data, repeated 10 times. We had previously calibrated the magnetic tweezer system using the same beads suspended in glycerol as described (Kollmannsberger and Fabry, 2007) to produce a 2D map of the force exerted on the bead based on the location relative to the tweezer tip. To calculate cytoplasmic viscosity, we rearranged Stokes' Law, which defines the drag force on a sphere moving through a viscous fluid:

$$\eta = \frac{F_d}{6\pi R v}$$

where F_d is the drag force, R is the bead radius, v is the bead velocity, and η is the effective cytoplasmic viscosity for particles similar in size to the magnetic bead. Final reported data points represent a calculation of cytoplasmic viscosity per pull across multiple cells. Errors were calculated taking into account tweezer calibration, bead localization, and the velocity fit.

Microscopy

Samples were imaged on an inverted Nikon Ti microscope equipped with a Yokogawa CSU-X1 confocal scanner unit with solid state 100-mW 488-nm and 50-mW 561-nm lasers, using a 60×1.4 NA plan Apo oil immersion objective lens, and a Hamamatsu ORCA R-2 Digital CCD Camera.

Samples with SiR-DNA/GFP-KDEL, FLAG-lipin/calnexin staining, cyclin A2/EdU staining, or telophase nocodazole washout cells were imaged on an inverted Nikon Ti Eclipse microscope equipped with a Yokogawa CSU-W1 confocal scanner unit with solid state 100 mW 405, 488, 514, 594, 561, 594, and 640 nm lasers, using a 60x 1.4 NA plan Apo oil immersion objective lens and/or 20x plan Fluor 0.75 NA multi-immersion objective lens, and a prime BSI sCMOS camera.

Samples for magnetic tweezer experiments and chromosome velocity measurements were imaged on an inverted Nikon Ti Eclipse equipped with a manual rotation stage. Multi-dimensional time-series images were acquired with a Yokogawa CSU-X1 spinning disk unit with a 1.2X camera mount magnifier, Coherent Obis lasers (488, 5660, 640 nm), a motor-driven filter wheel (filters: 514/60, 593/40, 647 LP; Ludl), an objective z-piezo stage (Physik Instrumente), a 60x 1.4 NA plan Apo oil immersion objective lens, and a sCMOS camera (Flash LT+, Hamamatsu).

Flow cytometry

Cells were plated into 2 wells of a 6-well plate per experimental measure with 250,000 cells/well. When indicated, cells were treated with 10 μM TOFA or DMSO for 24-48 hrs. Cells were labeled with 10 μM bromodeoxyuridine (BrdU) for 30 min, then washed twice with PBS and once with 3 mM EDTA in PBS, then incubated in 3 mM EDTA in PBS for 5-10 min before harvest by cell scraping and centrifugation. Pellets were resuspended in 100 μl in PBS and fixed with dropwise addition of 95% ethanol while vortexing. Samples were centrifuged and ethanol aspirated; samples were then incubated in 2N HCl with 0.5% Triton X-100 for 30 min, then centrifuged and supernatant decanted. Samples were incubated in 0.1 M sodium tetraborate decahydrate, pH 8.5 for 30 min, then centrifuged and decanted. Samples were stained with 1:200 mouse α BrdU in 1% BSA 0.2 % Tween-20 in PBS for 30 min, then centrifuged

Developmental Cell
Article

CellPress

and decanted, then washed with 1% BSA in PBS. Samples were stained with 1:200 FITC goat α mouse in 1% BSA 0.2 % Tween-20 in PBS, then centrifuged and decanted and washed with 1% BSA 0.2 % Tween-20 in PBS. Cells were resuspended in 100 μl of 100 μg/ml RNAse A in PBS and incubated for 5 min before addition of 400 μl 50 μg/ml propidium iodide in PBS. Samples were stored at 4 °C and analyzed within 24 hours. Samples were pushed through mesh filters just before analysis. All centrifugation steps were performed at 500 x g for 5 min, and all staining steps were performed on an orbital shaker.

Samples were analyzed on a Becton Dickinson LSR Fortessa using FACS DiVA software. Voltage settings used were: FSC 10, SSC 160, FITC 420, PE Texas Red, 300. 5000 events per experimental measure were recorded. Unstained and minus-one controls were included. Compensation between PE Texas Red and FITC channels was determined using FlowJo 10 using the traditional spillover algorithm.

To quantify the percentage of cells in G1, S, and G2 phase using FlowJo 10, singlet cells were first separated by gating the range from 2N-4N peaks in propidium iodide signal (Cecchini et al., 2012). The FITC-BrdU-positive (S) population gate was drawn using the minus-propidium iodide control, and the G1 and G2 populations were gated by drawing boxes around the 2N and 4N FITC-negative populations (Cecchini et al., 2012). Percentages are expressed as percentage of the singlet population.

Image analysis
Image analysis was performed using FIJI/ImageJ (Schindelin et al., 2012) unless otherwise noted. All images with multiple markers in the same image are composites (multiple markers shown as different colors in composites).

All data of ER phenotypes quantified by categorization were scored blindly. Images were blinded for analysis using the ImageJ Macro ImageJ Filename_Randomizer. For scoring of ER phenotypes, cells expressing moderate levels of GFP-KDEL with no overexpression artifacts (dense fluorescent clumps in ER or nuclei) were included for analysis. For scoring of interphase ER expansion, cells with a network of peripheral ER tubules visualized with GFP-KDEL or calnexin staining were considered "normal", whereas cells with ER sheets and tubules extending into the periphery with a lack of any tubular network were considered to have "expanded ER". In addition, cells with the appearance of thin ER tubules, large gaps between tubules, and a smaller cluster of perinuclear ER were considered to have "reduced ER" with TOFA treatment. In cells knocked down of lipin 1, the presence of ER sheets in the cell periphery was additionally blindly scored, where cells having multiple small, bright sheets within the tubular peripheral network were considered to have the "abnormal sheets" phenotype.

ER phenotypes were additionally quantified with percent abundance of cytoplasmic KDEL/calnexin signal or total ER area (cell cycle analyses of ER size). For cells with the entire ER captured within 0.3-0.5 μm interval z stacks, 8-bit maximum intensity projections were made of the whole field of view. To ensure the different ER morphologies were all accounted for after thresholding, the 8-bit max projections were subject to unsharp masking with a radius of 2 and mask of 0.6. The max intensity projection was thresholded using the Huang threshold of object fuzziness (Huang and Wang, 1995). The cell border and nuclear border for each cell were manually traced using ER fluorescent signal. For percent occupancy of the cytoplasm by ER membranes, the percent of pixels within the nucleus-free cell area that were GFP-KDEL(+) or calnexin(+) was measured. For ER area, the total area of calnexin signal in the nucleus-free cell area was measured. For calculation of cell area, the area within the cell border described above was used. For cell cycle staging, cells containing EdU punctae in the nucleus were considered to be in S phase. Cells with no EdU staining and nuclear cyclin A2 < cytoplasmic cyclin A2 were considered to be in G1 phase, whereas cells with no EdU staining and nuclear cyclin A2 $\geq$ cytoplasmic cyclin A2 were considered to be in G2 phase.

For quantification of micronuclei, images taken at 60x were scored for presence of micronuclei (DNA fragments encased in an emerin or calnexin-positive rim apart from main nucleus <~20% in size of the main nucleus). Severely lobulated/partitioned "hypermicronucleated" nuclei (DNA fragments/lobes apart from the main nucleus >~20% in size of the main nucleus) and micronuclei were scored through oculars or in 60x images of cells with nuclear envelope staining. Nuclei with both lobes/partitions and micronuclei were considered hypermicronucleated. For quantification of peripheral chromosome/tubulin masses in cells subjected to short-term nocodazole washout, 60× images of cells processed for immunofluorescence without non-kinetochore MT depolymerization were scored for the presence of chromosome masses with MTs extending to them that were away to the cell periphery compared with the primary nuclei chromosome masses.

Nuclear solidity was quantified as described (Fonseca et al., 2019). Briefly, DAPI/Hoechst images were thresholded with the ImageJ default setting, then the magic wand tool was used to select segmented nuclei. Nuclei that were unable to be segmented due to poor signal:noise, adjacent nuclei touching, or presence of a micronucleus touching the main nucleus were not included in the analysis. Segmented and selected nuclei were measured using the ImageJ shape descriptors measurement metric, which includes object solidity (the area fraction of a convex hull for an object). Data were expressed as % of nuclei with a solidity value less than the control U2OS average minus 1 standard deviation (Fonseca et al., 2019).

To quantify the percent of mitotic cell diameter that is occupied by ER membranes in cells expressing GFP-Sec61β/H2B-mCherry or GFP-KDEL/SiR-DNA, 60x image stacks of cells at anaphase onset (determined by first frame of visible chromatid separation) were obtained. Image background was subtracted using the average value of 3 boxes from surrounding the cell (but not within adjacent cells). A 10-pixel thick line was drawn encompassing the cell diameter along the metaphase plate (in the center of the dividing chromatin masses, along the division plane), and a profile plot was generated. The local maxima of the Sec61β/KDEL peaks for each side of the cell was determined, and the width of the half maxima for each of the 2 Sec61β/KDEL peaks was quantified and added together. This value was divided by the diameter of the cell (determined by the bounds of the Sec61β/KDEL half maxima) to determine the % of the cell diameter occupied by ER signal. For representation, plot profiles shown are normalized to minimum and maximum of

ER (stably expressed GFP-Sec61β/transiently expressed GFP-KDEL) and DNA (stably expressed H2B-mCherry, when applicable) signal.

For quantification of intracellular ER membranes in prometaphase-metaphase cells (determined by DIC chromosome appearance), 90x images of cells expressing GFP-KDEL and subject to mitotic shakeoff were blindly scored for presence of a) no intracellular ER membranes ("cleared"), (b) few ER tubules within the cell interior ("partially cleared"); or c) large (>2 μm length) sheets and/or several tubules within the cell interior ("not cleared").

To analyze average chromosome velocity in prometaphase cells, we used PIVlab, an open-source MATLAB toolbox for particle image velocimetry (Thielicke, 2014; Thielicke and Stamhuis, 2014), to generate velocity fields of chromosome movement within the chromosome mass. We then used MATLAB to filter and analyze velocity information. Final reported chromosome movements correspond to the average velocity magnitude of the chromosome mass deformation per frame averaged over time.

To measure nuclear localization of lipin, cells were blindly scored for localization of lipin 1 in 3 categories: mostly nuclear lipin 1, nuclear lipin 1 = cytoplasmic lipin 1, and mostly cytoplasmic lipin 1. Cell cycle staging was determined using cyclin A2 nuclear staining and EdU staining. For determining the cell cycle-specific localization of lipin 1, data were expressed as percentage of cells with nuclear lipin 1 (including both categories "mostly nuclear lipin 1" and "nuclear lipin 1 = cytoplasmic lipin 1").

QUANTIFICATION AND STATISTICAL ANALYSIS

GraphPad Prism 8 was used for all statistical analysis. Continuous data were tested for normality using a Shapiro-Wilk test. In imaging experiments where phenotypes of individual cells are scored, n refers to individual cells, unless otherwise defined. All N refer to experimental repeats. For experimental setups in which > 10 samples (n) per experimental replicate (N) were able to be collected consistently, continuous data were measured with paired t tests of experimental replicate means. Superplot format (Lord et al., 2020) was used for representing percent of ER-positive pixels in cytoplasm area and ER area. Experimental replicates of discrete data were plotted with shapes indicating separate replicates to display reproducibility, and incidences between groups (replicates pooled) were tested for significance using Fisher's exact test (2 categories) or Chi square test (>2 categories). Statistical tests used, sample sizes, definitions of n and N, and p values (p<0.05 as significance cutoff) are reported in figures and/or figure legends. For quantification of all data where >10 samples could be gathered within an experimental repeat, sample size calculations using the online tool (https://clincalc.com/stats/samplesize.aspx) determined the adequate sample size for number of cells to analyze for sufficient (80%) power.